Title

The Very Near Field of Three-Stream Jets

Author

Adam Alberdi, Andres Manuel

Publication Date

2018

UNIVERSITY OF CALIFORNIA,
IRVINE

The Very Near Field of Three-Stream Jets

THESIS

submitted in partial satisfaction of the requirements
for the degree of

MASTER OF SCIENCE

in Mechanical and Aerospace Engineering

by

Andres Manuel Adam Alberdi

Thesis Committee:
Professor Dimitri Papamoschou, Chair
Professor Feng Liu
Professor Roger H. Rangel

2018

TABLE OF CONTENTS

LIST OF FIGURES

LIST OF TABLES

NOMENCLATURE

Roman Symbols

$\mathbf{u}$	velocity vector
A	exit area
a	speed of sound
D	diameter
f	frequency
G	magnitude of mean velocity gradient
g	principal component of the Reynolds stress
k	wavenumber
M_c	convective Mach number
p	pressure
R	space-time correlation
r	radial location
S	spectral density
Sk	normalized skewness of the pressure fluctuation
Sr	Strouhal number
t	time
U	fully-expanded velocity
u, v, w	velocity components in Cartesian coordinate system
U_c	convective velocity
x, y, z	Cartesian coordinate system
BEM	Boundary-Element method

LES	Large Eddy Simulations
RANS	Reynolds-Averaged Navier-Stokes
SPL	sound pressure level

Greek Symbols

α	acoustic wavenumber
θ	polar angle relative to downstream jet axis
ϑ	direction cosine
κ	threshold value
ν_T	turbulent viscosity
ρ	density
τ	time delay
ϕ	azimuth angle
ξ	axial separation
ω	angular frequency

Subscripts

∞	ambient
p	primary (inner) stream
rms	root-mean-square
s	secondary (middle) stream
t	tertiary (outer) stream
wp	wavepacket

Superscripts

$'$	fluctuation with respect to the average value in time

ACKNOWLEDGMENTS

First and foremost, I would like to thank my advisor, Professor Dimitri Papamoschou, for his invaluable guidance through this work. He built the foundations for this thesis and introduced me to the field of aeroacoustics, which has captured my interest for good.

I would also like to profoundly thank Pete Balsells, founder of the Balsells Fellowship program, and its director Professor Roger Rangel for giving me the opportunity to come to the University of California, Irvine. They have contributed to mine and many more people's growth, not only career-wise, but also personal.

The support by NASA Cooperative Agreement NNX14AR98A, monitored by Dr. James Bridges, is gratefully acknowledged.

I want to thank my laboratory partners, especially Dr. Vincent Phong, who provided the first light when I first met the field of aeroacoustics. Also thanks to my friends, many of whom are also Balsells fellows, for sharing the experience and building a new home in California.

I must thank my parents and my sister for their unconditional, relentless support.

Portions of the text of this thesis are a reprint of the material as it appears in "The Very Near Pressure Field of Three-Stream Jets." I thank the co-authors of this publication, Professor Dimitri Papamoschou, Dr. Juntao Xiong and Professor Feng Liu. In addition, their role in providing a theoretical background without which this thesis would not exist is greatly appreciated.

ABSTRACT OF THE THESIS

The Very Near Field of Three-Stream Jets

By

Andres Manuel Adam Alberdi

Master of Science in Mechanical and Aerospace Engineering

University of California, Irvine, 2018

Professor Dimitri Papamoschou, Chair

Large eddy simulations (LES) of two hot three-stream jets are used to assess key assumptions made in recent volumetric and surface-based models of jet noise sources based on Reynolds-Averaged Navier Stokes (RANS) flow fields, and to explore the proper definition of a linear surface-based model. The jets studied are at the conditions of a supersonic turbofan engine at takeoff.

A new method for the detection of the RANS-based surface of peak stress (OSPS) for an eccentric jet is employed. Direct measurements of the Reynolds stress and convective velocity show that the RANS-based OSPS and convective velocity are in good agreement with the LES results. In addition, evaluation of the instantaneous pressure fields suggests that the most energetic events happen at the OSPS. These results lend credence to the use of the RANS-based OSPS to simulate the convective Mach number distribution in a multi-stream jet.

Efforts are made on the study of the proper location of a "radiator surface" for a linear surface-based model. This surface follows the "edge" of the jet, defined as the boundary between the rotational and irrotational fields. Previously employed definitions for the location of this surface based on thresholds of the gradient of mean axial velocity place it too far on the acoustic field, and therefore fail to produce a surface with the desired property.

A surface on which the convective velocity matches that on the OSPS falls exactly on this boundary. This surface also appears to follow the outer band of a layer of negative pressure skewness on both of the nozzles studied.

Chapter 1

Introduction

1.1 Motivation

Aircraft noise is nowadays one of the main sources of noise pollution, especially in urban areas. It has concerned the aerospace community for more than sixty years and its relevance has done nothing but increase with time. Already in 1969, the Federal Aviation Administration issued noise standards for new designs of civil subsonic jet aircraft. During the subsequent years to date, new and stricter steps of noise regulation have been adopted, making aircraft noise generation one of the biggest challenges for the aerospace community today.

Constraints for maximum aircraft noise generation are not unfounded. Aircraft noise creates economic and health impacts for both airports and their neighboring population. A study of 181 airports around the world by Kish[4] estimated a total of $21 billion in housing value loss and $800 million in rent loss only during the year 2005. The same study also estimated the amount of people exposed to 55 dB in 14 million, and 2.3 million people highly annoyed. This can cause an impact on their health, as studies suggest that aircraft noise has an impact on individuals' cognitive abilities[5] and is associated with and increase in heart problems.[6] Overall, aircraft noise reduction leads to better integration with the population living near airports, improving air transportation and making a valuable contribution to society.

Noise reduction becomes crucial for the development of commercial supersonic aviation. The engines of this new generation of aircraft are found to be key aspects to study, being one of the main sources of noise while also the basis for supersonic flight. This leads to innovative, powerful three-stream turbofan engines carefully crafted to be as silent as possible. In the process of making such engines a reality, the designing steps need to be as efficient and reliable as possible, therefore allowing iterative design processes to achieve maximum optimization. Turnaround times for noise assessments become then of the order of days or hours. For this reason, they must be obtained from prediction models instead of the first-hand alternatives, which result too slow and inconvenient. One of the main possibilities for rapid jet noise predictions is to base them on Reynolds-averaged Navier-Stokes (RANS) simulations and use assumptions on the time-averaged data obtained to account for noise generation. However, these assumptions need to be thoroughly verified with time-resolved methods to ensure their validity. It is the main purpose of this work to help verify key assumptions for RANS-based noise prediction models for three-stream jets, as well as understanding the physics behind the noise generation of this new type of engine. This is an extended version of the work presented in Ref. 7.

1.2 Previous Work

1.2.1 Components of Jet Noise

Jet noise is caused by three different phenomena: turbulent mixing noise, screech tones, and broadband shock-associated noise. The last two exist on nozzles on supersonic operation when the exit pressure is not perfectly matched the ambient pressure, while the first is present both in subsonic and supersonic operations. Figure 1.1 shows a typical noise spectrum of a non-perfectly expanded supersonic jet measured experimentally by Seiner.[1] In this figure the Sound Pressure Level (SPL) is plotted versus the non-dimensional frequency (Strouhal number St). It is very outstanding a high peak of discrete frequency near $St = 0.4$. This is also called screech tone, and often appears with more than one harmonic. To its right is the broadband shock-associated noise, and to its left is the turbulent mixing noise. Frequencies and intensities of these three natures depend on the conditions of the jet, geometry of the nozzle, and position of the observer.

When a nozzle is operated at off-design, supersonic conditions, shock or expansion waves are formed at the lip due to the mismatch of the static pressures inside and outside the jet. These waves reflect continuously along the flow creating a diamond-pattern shape called shock-cell structure. This is the cause for the two shock-associated noise sources, broadband and screech. Broadband shock-associated noise is generated by the interaction between the downstream propagating large turbulent structures of the jet flow and the shock cell structure.[8] Screech tones are believed to be product of an acoustic feedback mechanism: acoustic disturbances excite the thin jet mixing layer near the nozzle lip. The amplitude of this instability grows with downstream propagation, then interacting with the shock cells in the jet plume. This interaction creates acoustic radiation which primarily propagates in the upstream direction outside the jet. The feedback loop is closed when the acoustic radiation reaches the nozzle lip region and excites the thin shear layer of the jet.[9] Fortunately, both

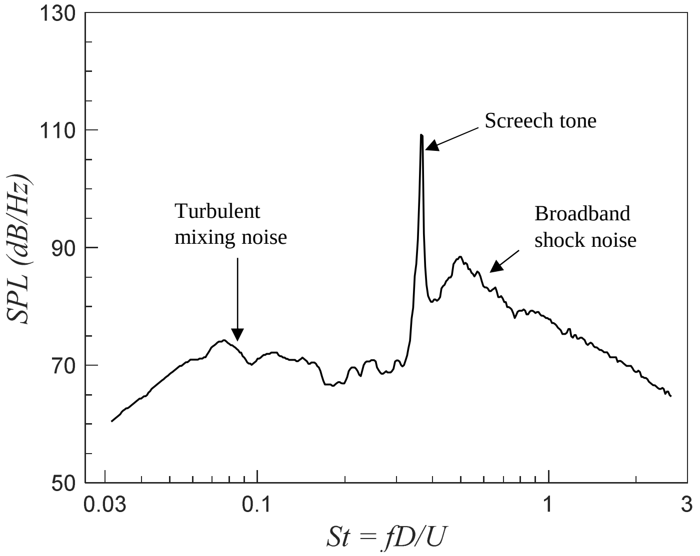

Figure 1.1: Typical far field noise spectrum from Seiner.[1] Microphone at 150° to downstream jet axis.

shock-associated noise components can be eliminated by matching the static pressures inside and outside the jet exit, a condition where shock-cell structures are not generated and the nozzle operates at optimum conditions. For this reason, and keeping in mind that this work deals with civil applications, it is more important to study the remaining component: turbulent mixing noise.

It is generally accepted that turbulent jet flows contain both fine- and large-scale turbulence structures, and that both of them generate noise. An extensive analysis of many jet noise spectra carried out by Tam *et al.*[10] divided the far-field noise in two similarity spectra which are arguably two different noise generation mechanisms, one for fine-scale and another for large-scale turbulence. Subsequent experimental work by Tam,[11] Dahl & Papamoschou,[12] and Viswanathan,[13,14] among others, supported such distinction over a large number of operating conditions, while also discussing the limitations of the similarity spectra modeled. Large-scale turbulence structures generate strongly directional noise which peaks at low angles to the downstream centerline. Noise generated by fine-scale turbulence is generally

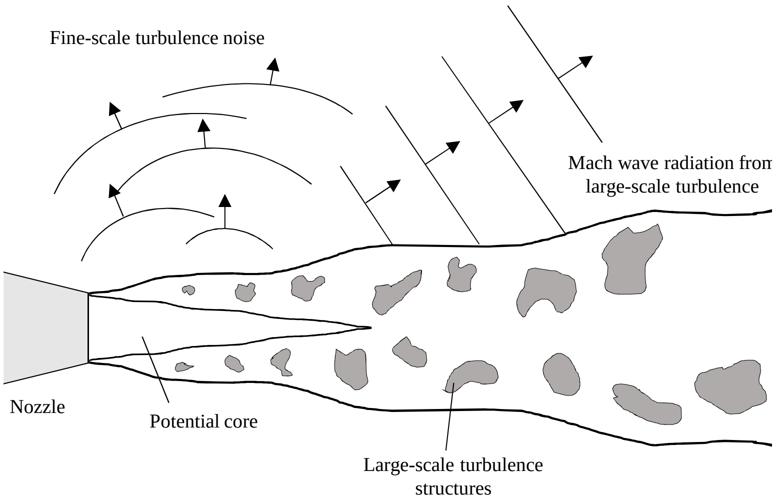

Figure 1.2: Diagram showing the turbulent mixing noise generation mechanisms in a single-stream jet.

omnidirectional. A schematic representation of these mechanisms is shown in Fig. 1.2. For their difference in directivity, fine-scale turbulence is the main mechanism for noise at large angles relative to the downstream centerline, but the large-scale turbulence is generally responsible for the absolute peak noise generation.

Brown and Roshko[15] were among the first to prove the existence of large-scale turbulence structures in two-dimensional shear layers, providing visualizations still greatly appreciated by the aerospace community. Since then, a number of studies analyzed the generation, growth and acoustic influence of these structures both theoretically[16,17,18] and experimentally.[19,20] The far-field noise emission of these structures can be explained by understanding their nature as linear instability waves, as shown by the theoretical work of Tam *et al.*[10] The most basic tool is to shift the frame of reference to the instability wave, where it behaves like a wavy wall on a moving flow. If the flow is supersonic, the disturbance on the wall creates Mach waves that propagate through the fluid as shown in Fig. 1.3. This would be the case for a instability wave moving with a speed that is supersonic relative to the ambient fluid. This can be seen in supersonic jets, where large-scale structures are clearly the dominant source of noise. However, studies by Tam *et al.*[10,21] and Viswanathan[13] have demonstrated that noise is generated by large-scale structures in all operating conditions, including subsonic speeds. The explanation for this phenomena relies on the growth and decay of the instability waves as they propagate downstream. Near the nozzle exit, the shear layer is thin and the mean-velocity gradient is large enough to cause linear instabilities to grow rapidly. As these grow downstream, the shear layer thickens and the mean-velocity gradient reduces, which then slows the growth of the linear instabilities until they stop growing at a certain point. On propagating further downstream the wave experiences damping until it disappears. This can be translated to the wavy wall analogy by adding a growth and decay of the wall "waves" acquiring the form of a "wavepacket". Reproducing the procedure from Papamoschou,[2] let $\eta(x,t)$ describe the vortex sheet between jet and a quiescent ambient or, in the wavy wall analogy, the shape of the wavepacket being

$$\eta(x,t) \;=\; A(x)e^{i(k_{wp}x-\omega_{wp}t)} \tag{1.1}$$

where x is axial position, t is time, k_{wp} is the wavepacket wavenumber, ω_{wp} is the wavepacket frequency and $A(x)$ is the envelope of the oscillations which determines the spatial growth and decay. U_c is the speed at which the instability moves downstream, called convective velocity, and is related to Eq. 1.1 by

$$U_c \;=\; \omega_{wp}/k_{wp} \tag{1.2}$$

The convective Mach number of the instability wave is

$$M_c \;=\; U_c/a_\infty \tag{1.3}$$

When the amplitude A is constant, the instability radiate far-field sound for $M_c \;>\; 1$ as explained before. The wavepacket can be represented by a superposition of traveling waves

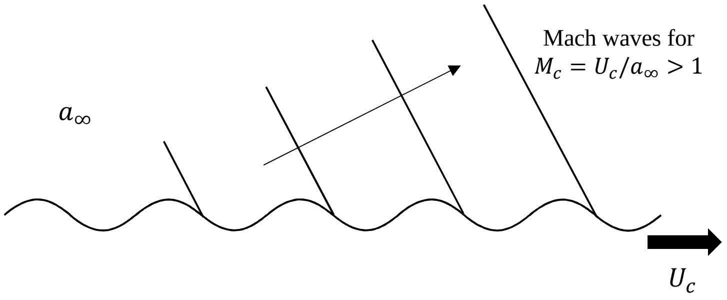

Figure 1.3: Mach wave emission in the case of a wavy wall moving with velocity U_c supersonic with respect to the ambient speed of sound.

in Fourier space as

$$\eta(x,t) \ = \ 1/2\pi \int_{-\infty}^{\infty} \hat{A}(k-k_{wp}) e^{i(kx-\omega_{wp}t)} dk \tag{1.4}$$

Therefore each individual wave has an amplitude in the Fourier space of $\hat{A}(k-k_{wp})$ and convective velocity of

$$U_{c,i} \ = \ \omega_{wp}/k \tag{1.5}$$

This means that the effect of growth and decay of instabilities transform the discrete frequency component of the perturbations into a wider wavenumber spectrum of waves traveling at different convective velocities. The convective Mach number for each wave is then

$$M_{c,i} \ = \ \omega_{wp}/k a_\infty \tag{1.6}$$

This results means that even though M_c given by Eq. 1.3 is subsonic, the spectrum of the waves conforming the wavepacket may have components of supersonic convective speed $|k| \ < \ \omega_{wp}/a_\infty$ that generate Mach wave radiation into the far field. Therefore the growth and decay of turbulence structures is a critical factor in their noise generation and their basic mechanism in subsonic flows. This effect is seen in their regions of main noise generation: the first few diameters if the nozzle exit and at the end of the potential core.

1.2.2 Effects of Multi-Stream Jets

Nowadays, the majority of engines for both commercial and military applications are two-stream turbofans. This not only allows for the increase in fuel efficiency that mainly motivated their use, but also for a significant reduction in the noise generated. The existence of a slower secondary flow surrounding the primary stream can reduce the Mach wave radiation of the jet by means of lowering the values of M_c of the turbulent structures responsible for their production.[2]

Figure 1.4 from Papamoschou[2] shows the basic elements of a two-stream jet flow. There is a primary shear layer between the primary and secondary cores, and a secondary shear layer between the secondary core and the surrounding fluid. The secondary core is determined by the inflection points in mean velocity *i2* and *i3*. All streams have an initial potential core which disappears with the expansion of the shear layers and the convection downstream of the flow. In the region where the secondary core exists, surrounding the primary core, the primary shear layer is silent. That way, only the slower moving turbulence structures created in the secondary shear layer are responsible for Mach wave acoustic emission during the first diameters downstream, "shielding" part of one of the most important areas of noise generation. In addition, the presence of a second exhaust offers the possibility of reshaping the nozzle geometry to reduce sound radiation in specific directions, focusing in the downwards and sideways directions for quieter operations of take off and landing.[22]

Advanced engine architectures of the last years offer three-stream arrangements for turbofans that enhance the efficiency and stability of the engine cycle and seem to be key for supersonic transports. The acoustic and fluid dynamics of these jets have received considerable attention in recent experimental and numerical studies.[3, 23, 24, 25] A tertiary exhaust allows even more configurations in the search for noise reduction together with a change in the overall flow and noise sources.

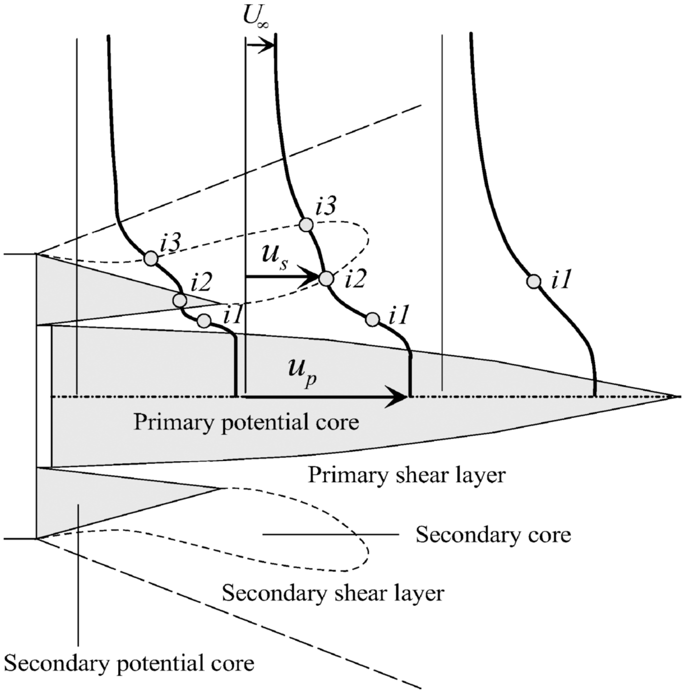

Figure 1.4: Basic elements of a two-stream jet, from Papamoschou.[2]

1.2.3 Modeling of Jet Noise

With community noise and exposure of military personnel to near-field sound becoming prominent factors in the design of new commercial and military engines, their design stages need to include rapid, reliable noise predictions that allow iterative designing processes. Aerospace industry and government agencies have requirements for low-cost prediction of aircraft engine noise, with turnaround times on the orders of hours.

Highly resolved computational tools, such as Large Eddy Simulations (LES) have been developed to the point where they can provide high-fidelity time-resolved solutions of the flow field. Together with surface-based integration methods, these computations can predict reliable far-field noise spectra. However, the computational time that they require makes them inconvenient as a design tool. Low-cost simulations, such as RANS, are the predominant tool for noise assessment with short turnaround times.

Jet noise RANS-based source modeling can take two forms, volumetric and surface-based. Both aim to address the noise generation caused primarily by large-scale turbulence structures on turbulent mixing noise, but use different methods to account for their effect. The basic characteristics of each one are briefly explained in the following paragraphs.

Volumetric Source Modeling

Volumetric source modeling was first initiated by Lighthill[26] in what is called *Acoustic analogy.* Using the fundamental equations of fluid mechanics, the mechanisms of noise generation inside the jet are modeled by a distribution of sources.

First, the equation of continuity can be written as

$$\frac{\partial \rho}{\partial t} \; + \; \boldsymbol{\nabla} \cdot \rho \mathbf{u} \; = \; 0 \tag{1.7}$$

where ρ is density and $\mathbf{u}$ is the vector of velocity. The equation of momentum can be written as

$$\frac{\partial \rho \mathbf{u}}{\partial t} \; + \; \rho \mathbf{u}\mathbf{u} \; + \; \nabla p \; - \; \boldsymbol{\nabla} \cdot \tau \; = \; 0 \tag{1.8}$$

where p is pressure and τ is the viscous stress tensor. Cross-differentiating and combining Eqs. 1.7 and 1.8, one obtains

$$\frac{\partial^2 \rho}{\partial t^2} \; - \; a_\infty^2 \nabla^2 \rho \; = \; \boldsymbol{\nabla} \cdot \boldsymbol{\nabla} \cdot \left[(p - a_\infty^2 \rho)\mathbf{I} \; + \; \rho \mathbf{u}\mathbf{u} \; - \; \tau \right] \tag{1.9}$$

where the term $a_\infty^2 \nabla^2 \rho$ was subtracted from both sides to render the left hand side as a wave operator. In the surrounding fluid, the propagation of the disturbances made by the sources to the far field is considered small and isentropic, so

$$p' \; = \; a_\infty^2 \rho' \tag{1.10}$$

where p' and ρ' are respectively the pressure and density fluctuations with respect to their mean values. Combined with Eq. 1.10, Eq. 1.9 becomes, in the linear region,

$$\frac{1}{a_\infty^2}\frac{\partial^2 p'}{\partial t^2} \;-\; \nabla^2 p' \;=\; \boldsymbol{\nabla}\cdot\boldsymbol{\nabla}\cdot\mathbf{T} \tag{1.11}$$

where $\mathbf{T}$ is the Lighthill stress tensor

$$\mathbf{T} \;=\; (p - a_\infty^2\rho)\mathbf{T} \;+\; \rho\mathbf{u}\mathbf{u} \;-\; \tau \tag{1.12}$$

The left hand side of Eq. 1.11 can be identified as a wave operator for p', and the right hand side is analogous to a source term, thus from here the expression "acoustic analogy". Owing to the double-divergence of the right hand side, Lighthill characterized the source term as a distribution of quadrupoles. In 3D free space, it can be solved using Green's function, yielding

$$p'(\mathbf{x},t) \;=\; \boldsymbol{\nabla}\cdot\boldsymbol{\nabla}\cdot\int_{\mathcal{V}}\mathbf{T}(\mathbf{y},t-\frac{d}{a_\infty})\frac{1}{4\pi d}d^3\mathbf{y} \tag{1.13}$$

Here $\mathbf{x}$ and $\mathbf{y}$ are spatial coordinates for the source and observer, respectively; $\mathcal{V}$ is the source region and $d = |\mathbf{x}-\mathbf{y}|$ is the distance between source and observer. Applying the chain rule and neglecting terms that decay faster than the inverse of the source-observer distance, the double spatial divergence is transformed into a second time derivative,

$$p'(\mathbf{x},t) \;=\; \int_{\mathcal{V}}\vartheta_i\vartheta_j\frac{\partial^2 T_{ij}}{\partial t^2}(\mathbf{y},t-\frac{d}{a_\infty})\frac{1}{4\pi d}d^3\mathbf{y} \tag{1.14}$$

where

$$\vartheta_i \;=\; \frac{x_i - y_i}{d} \tag{1.15}$$

The notation was switched to index notation for convenience. Eq. 1.14 is an expression for acoustic pressure everywhere. The neglected terms that decay faster than d^{-1} conform the hydrodynamic pressure. However, volumetric modeling is not aiming to solve for p' but for the power spectral density. The spectral density of the acoustic pressure is obtained from the Fourier transform of the autocorrelation

$$S(\mathbf{x},\omega) \; = \; \int_{-\infty}^{\infty} \overline{p'(\mathbf{x},t)p'(\mathbf{x},t \; + \; \tau)} e^{-i\omega\tau} d\tau \tag{1.16}$$

Inserting Eq. 1.14 in Eq. 1.16 yields

$$S(\mathbf{x},\omega) \; = \; \frac{\alpha^4}{16\pi^2} \int_{\mathcal{V}} \int_{\mathcal{V}} \int_{-\infty}^{\infty} [\vartheta_i \vartheta_j \vartheta'_k \vartheta'_l] R_{ijkl}(\mathbf{y},\mathbf{y}',\tau) \frac{\exp[i\alpha(d-d') - i\omega\tau]}{dd'} d\tau d^3\mathbf{y}' d^3\mathbf{y} \tag{1.17}$$

where

$$R_{ijkl}(\mathbf{y},\mathbf{y}',\tau) \; = \; \overline{T_{ij}(\mathbf{y},t) T_{kl}(\mathbf{y}',t+\tau)} \tag{1.18}$$

is the space-time correlation of the Lighthill stress tensor, $d' = |\mathbf{x}' - \mathbf{y}'|$, and $\alpha = \omega/a_\infty$ is the acoustic wavenumber. This development was first carried by Lighthill, and was reproduced here following the notation and methodology of Papamoschou.[3] From this point on, the effort is centered in modeling the term R_{ijkl} and the methodology to do so differ between researchers. This work uses the development of Papamoschou.[3] The correlation R_{ijkl} is modeled as

$$R_{ijkl}(\mathbf{y},\mathbf{y}',\tau) \; = \; A_{ijkl} \; R_1 \; R_{23} \; R_4 \tag{1.19}$$

where A_{ijkl} is the amplitude of the correlation; R_1 and R_4 are axial and timewise correlations, respectively; and R_{23} is a mixed radial/azimuthal correlation (the arguments are omitted for conciseness). The behavior of each term is studied and their terms of dependence are estimated. Key parameters of the modeling, such as time and length scales, are obtained from the RANS solution. The construction of time and length scales involves “tuning” parameters that are obtained from knowledge of the acoustics of a baseline jet.

The timewise integration in Eq. 1.17 amounts to a Fourier transform in the time separation τ. On applying far-field approximations (which include $d'd \approx d^2$) and considering the slow axial development of the flow, the 3D spatial integration over $\mathbf{y}'$ contains an axial integral that also amounts to a Fourier transform. These transformations affect the terms R_1 and R_4, so the compact form of the spectrum is

$$S(\mathbf{x}, \omega) = \frac{\alpha^4}{16\pi^2 d^2} \int_{\mathcal{V}} A_{0000} \tau_* L_1 \pi L_{23}^2 \hat{R}_1 \hat{R}_4 \tilde{R}_{23} d^3\mathbf{y} \tag{1.20}$$

A_{0000} is the amplitude of the projection of R_{ijkl} along the observer direction; τ_*, L_1, and L_{23} are timewise, axial, and transverse correlation length scales respectively; $\hat{R}_1$ and $\hat{R}_4$ are the Fourier transforms of the axial and timewise correlations; and $\tilde{R}_{23}$ is the Hankel transform of the cross-stream correlation. The detailed derivation can be found in Ref. 3.

Terms R_1 and R_4 of Eq. 1.19 are dependent on the convective velocity of turbulent eddies U_c. Particularly R_1, whose Fourier transform appears in 1.20 and has the argument

$$\hat{R}_1[\alpha L_1(\tfrac{1}{M_c} - cos\theta)]$$

This term is called *radiation efficiency* and is very important in understanding the noise radiation generated by large-scale turbulence structures. For $M_c > 1$, the radiation efficiency peaks at $cos\theta = 1/M_c$, where the argument of R_1 is zero. This represents the Mach wave emission in high speed jets, so the peak noise generation is near $\theta = arcos(1/M_c)$. For $M_c < 1$, the radiation efficiency increases monotonically towards $\theta = 0°$. However, the validity of this modeling is limited to angles higher than the spreading of the flow, around $\theta = 10°$. Sound emission at lower angles can be influenced by flow-acoustic interactions. The importance of the radiation efficiency term and its connection with the large scale turbulence structures make the modeling of convective velocity critical for the accuracy of the model. The assumptions made for this are explained later in this subsection.

Surface-based Modeling

In surface-based modeling, flow and propagation are separated. The jet noise source is modeled from low-cost simulations and prescribed on a "radiator surface", placed on the boundary between the inner rotational flow field and the outer linear pressure field. The propagation is then computed using well established linear tools, such as the Boundary Element Method (BEM). This method of modeling allows not only an estimation of the far-field noise in a free space, but also allows accounting for near-field noise and scattering on surfaces, which can simulate the structure of the plane. The methodology used here was presented by Papamoschou *et al.*[27]

The pressure field on the radiator surface is prescribed by partial fields that model the effects of large-scale turbulent structures in the jet region, convecting downstream and mixing with an inherent stochastic nature, as shown in Fig. 1.5. The partial fields acquire the shape of wavepackets. Just outside the jet, the pressure distribution reflects the "footprint" of the turbulent eddies responsible for sound generation.[28,29] Therefore, the pressure events on the radiator surface that will determine noise generation on a BEM simulation will be strongly linked to the turbulent eddies on the vortical field, and are expected to have similar coherence scales and convective velocity.

Length scales and convective velocity distribution need to be obtained from low cost RANS simulations, which is done the same way as with the volumetric source modeling. In addition, it is crucial for this model to reflect the stochastic nature of turbulent eddies, where Papamoschou has made advances in Ref. 30; and to obtain the correct location of the radiator surface.

For a computation of the noise propagation, any surface that does not contain the vortical field and correctly accounts for the pressure events in that location can be used as a source. However, there is only a thin region outside the jet that contains the full information emitted,

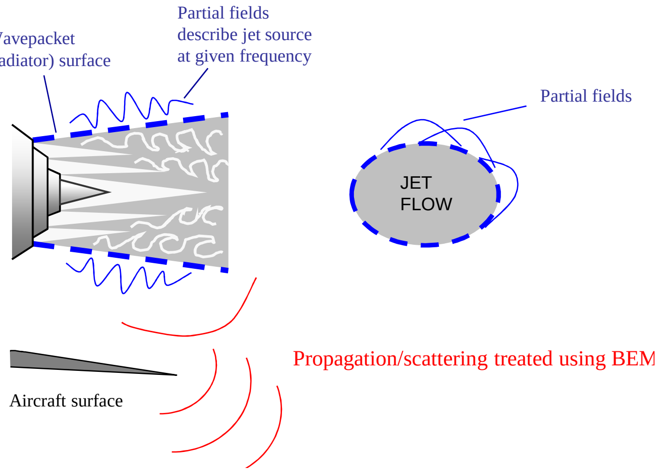

Figure 1.5: Basic elements of surface-based modeling of the jet noise source.

that is, both acoustic and hydrodynamic components of pressure. The latter is considered the signature of the turbulence eddies of the jet and decays rapidly outside of it. Therefore, that region is the connection between the turbulence field and the linear pressure field, defined as the *edge* of the jet. Because in this model the radiator surface is built based on the effects of turbulent structures, it should be placed on that edge. Small inaccuracies in its placement can be considered to have negligible effect on far-field noise in free space propagation, but they might have an important effect on near-field noise and scattering applications.

In the following it is used the cylindrical coordinate system $\mathbf{x} = (x, r, \phi)$ where x is the axial coordinate, r is radial coordinate and ϕ is the azimuthal angle. The criterion for determining the edge of the jet used in Ref. 27 is based on the radial gradient of mean axial velocity $\partial\overline{u}/\partial r$, such that

$$\frac{\partial\overline{u}/\partial r}{(\partial\overline{u}/\partial r)_{max}} \to 0 \tag{1.21}$$

where $(\partial\overline{u}/\partial r)_{max}$ is the value where the radial gradient reaches the outermost maximum. The location r_{edge} of the edge of the jet is practically defined where

$$\frac{|\partial\overline{u}/\partial r|(x, \phi, r_{edge}(x))}{|\partial\overline{u}/\partial r|_{max}(x, \phi)} = \kappa \tag{1.22}$$

where κ is a threshold value $\kappa << 1$. However, this definition results impractical to find both numerically and experimentally, because at low values of $\partial\overline{u}/\partial r$, noise in the measurements becomes relevant and the accurate location of the surface becomes complex. In addition, the validity of this definition still needs to be verified for three-stream jets.

Modeling of Convective Velocity

It has been mentioned that both volumetric and surface-based modeling need to account for the convective velocity of the large-scale turbulent structures inside the vortical field. Direct calculation of this magnitude is impossible from the time averaged data given by RANS simulations, so it needs to be modeled from the information available. For this matter, it is important to look at the nature of the turbulence eddies: their main contribution is the transport of quantities such as momentum, heat, species, etc. across the jet. Focusing on the momentum transport, in a statistical sense that effect is captured by the velocity correlation $\overline{\mathbf{u'u'}}$, or the associated Reynolds stress tensor $\overline{\rho}\overline{\mathbf{u'u'}}$. It is postulated by Papamoschou[3] that the turbulent structures induce the largest contributions in, and therefore are best represented by, the Reynolds stress. For this effect, we use the constitutive relation that defines the backbone of turbulence modeling[31]

$$\overline{u_i'u_j'} \;=\; \frac{2}{3}k\delta_{ij} \;-\; \nu_T S_{ij} \tag{1.23}$$

where ν_T is the turbulent viscosity and

$$S_{ij} \;=\; \frac{\partial\overline{u}_i}{\partial x_j} \;+\; \frac{\partial\overline{u}_j}{\partial x_i} \tag{1.24}$$

The dominant component of S_{ij} is the transverse gradient of the mean axial velocity. The approximate magnitude of this gradient is

$$G = \sqrt{\left[\frac{\partial \overline{u}}{\partial y}\right] + \left[\frac{\partial \overline{u}}{\partial z}\right]} \tag{1.25}$$

where y and z are part of a Cartesian coordinate system $\mathbf{x} = (x, y, z)$, x is the axial centerline of the jet in the downstream direction and y, z are transverse components. The azimuthal angle ϕ is defined such that $\phi = 0°$ is pointing to the negative direction of y. The azimuthal direction of the gradient of Eq. 1.25 is defined as ϕ_g.

It is argued that the principal turbulent transport is in the direction of the mean flow gradient. Neglecting is axial component, it is associated with a traverse velocity fluctuation q'. The corresponding velocity correlation

$$g = < u'q' > = \nu_T G \tag{1.26}$$

is considered the main contributor to the transport and hence to the Reynolds stress. The correlation g is loosely referred to as the "Reynolds stress" and treated as non-negative.

As mentioned in section 1.2.2, the outermost turbulent eddies are the main contributors to Mach wave radiation and its associated peak noise. Accordingly, it is defined the outer surface of peak stress (OSPS) as the locus of the peak Reynolds stress as one approaches the jet from the ambient towards the jet axis. Denoting the radial location of the OSPS as $r_{OSPS}(x, \phi)$, the convective velocity of the turbulent eddies is modeled as the mean axial velocity at the OSPS, or

$$U_c(x, r, \phi) = \overline{u}(x, y_{OSPS}(x, \phi), \phi) \tag{1.27}$$

1.3 Objectives

The research detailed in this thesis is focused on verifying key assumptions made in previous efforts for the creation of RANS-based noise prediction models with highly resolved LES of three-stream jets. The objectives of the study include:

- Comparison of LES and RANS flow fields of three-stream jets.
- Comparison of LES- and RANS-based outer surfaces of peak stress (OSPS).
- Verification of RANS-based model for convective velocity using space-time correlations on LES data.
- Investigation on the proper location of a radiator surface for linear-based modeling.

1.4 Thesis Overview

- **Chapter 1:** Introduction of topic of interest.
- **Chapter 2:** Outline of the conditions, geometries and properties of the simulations.
- **Chapter 3:** Location of the OSPS and comparison of convective velocity.
- **Chapter 4:** Location and verification of the radiator surface.
- **Chapter 5:** Summary of the findings in this study.

Chapter 2

Jet Flow

Two three-stream jets are analyzed, named AXI04U and ECC09U. They are based on nozzle systems being developed and NASA John H. Glenn Research Center (GRC)[32] and have been studied in previous works.[33] Both are externally-mixed, externally-plugged convergent nozzles. Their design specifications are depicted in Fig. 2.1. The subscripts p, s and t refer to the primary (inner), secondary (middle) and tertiary (outer) streams, respectively. Both nozzles are designed with the same area-based exit diameter of the primary duct $D_{p,eff} = 13.33$ mm. Their secondary-to-primary and tertiary-to-primary area ratios are also common, $A_s/A_p = 1.44$ and $A_t/A_p = 1.06$ respectively. AXI04U is an axisymmetric design, while ECC09U has an eccentricity on the tertiary flow, of thickness $h_t(\phi)$. Where ϕ is the azimuthal angle denoting the "downwards" direction with $\phi = 0°$. Nozzle ECC09U incorporates a wedge-type deflector centered at $\phi = 180°$ of side length L and half angle δ. This creates the thickness distribution visible in Fig. 2.1. Compared to AXI04U, nozzle ECC09U has a thicker tertiary flow at the regions $0° \leq \phi < 110°$ and $250° < \phi \leq 360°$. At the upper half of the nozzle, the thickness gradually reduces until it is suddenly suppressed between the angles $160 \leq \phi \leq 200°$

Table 2.1: Cycle point.

Primary			Secondary				Tertiary			
NPR$_p$	NTR$_p$	U$_p$, m/s	BPR$_s$	NPR$_s$	NTR$_s$	U_s/U_p	BPR$_t$	NPR$_t$	NTR$_t$	U_t/U_p
2.02	3.38	590	2.33	2.02	1.34	0.63	1.31	1.53	1.24	0.48

Nozzle AXI04U was chosen for this study because it is an axisymmetric concept with some noise reduction modifications: shortened cowl and enlarged plug. It has given promising results for noise reduction and has been the base for new eccentric nozzle concepts. Its geometry is detailed in Fig. 2.2. Nozzle ECC09U is based on AXI04U and has given reasonably good results of noise reduction in the downwards ($\phi = 0^\circ$) direction. In Fig. 2.2 and in the following sections, the axial coordinate x has the origin at the tip of the plug and is positive towards the downstream direction.

Both nozzles were operated at the cycle conditions listed in Table 2.1, which represents exhaust conditions for a supersonic engine turbofan engine at takeoff. The symbol U refers to the exit (fully-expanded) velocity; the nozzle pressure ratio (NPR) is the ratio of the jet stagnation pressure to ambient pressure; the nozzle temperature ratio (NTR) is the ratio of the effective (density based) jet stagnation temperature to ambient temperature; and the bypass ratio (BPR) is the ratio of either secondary or tertiary stream mass flow rate to the primary stream mass flow rate. The Reynolds number based on the conditions of the primary stream and $D_{p,eff}$ was 1.8×10^5.

2.1 Computational Details

Two types of computations were applied to jets AXI04U and ECC09U: Reynolds-Averaged Navier Stokes (RANS) and Large Eddy Simulation (LES). Both were conducted at the cycle conditions listed in Table 2.1 and at the Reynolds number $Re = 1.8 \times 10^5$ of the subscale

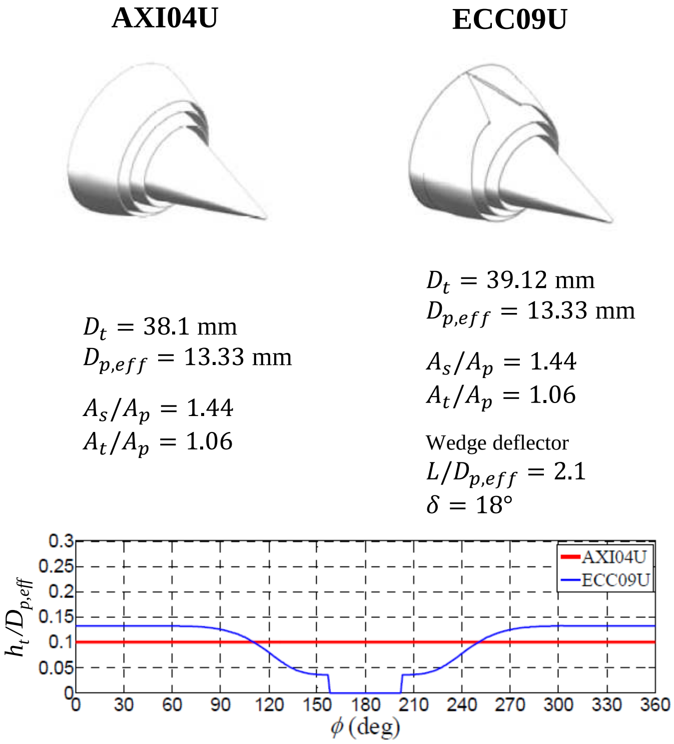

Figure 2.1: Nozzle exit design specifications, including the azimuthal variation of the tertiary annulus width.

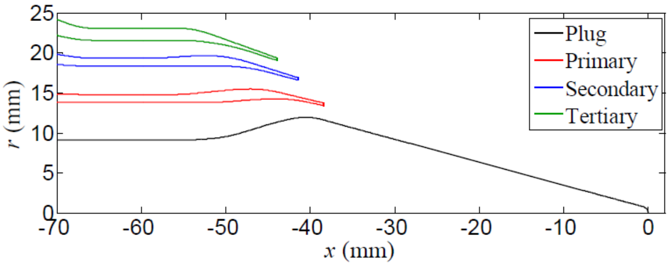

Figure 2.2: Radial coordinates of nozzle AXI04U.

experiments[33] (based on the primary exit conditions and $D_{p,eff}$. The main elements of the numerical codes are summarized below.

2.1.1 RANS

The computational fluid dynamics code used in this project is known as PARCAE,[34] which has been applied to similar nozzles.[25,35] The code solves the unsteady three-dimensional Navier-Stokes equations on structured multiblock grids using a cell-centered finite-volume method. Information exchange between multiblock grids is implemented through MPI (Message Passing Interface) protocol. A time-averaged implementation of this code is used on this work, where it solves the RANS equations using the Jameson-Schmidt-Turkel dissipation scheme[36] and the Shear Stress Transport (SST) turbulence model of Menter.[37] The governing equations were solved explicitly in a coupled manner using five-stage Runge-Kutta scheme toward steady state with local time stepping, residual smoothing, and multigrid techniques for convergence acceleration. Only the steady-state solution was considered because we are interested in the time-averaged features of the flow.

The computation encompassed both the internal nozzle flow as well as the external plume. The computational domain extended to $30D_t$ axially and $8D_t$ radially. In order to save computational resources, the symmetry of the flow was used and only one half of it was simulated. For all three streams, uniform total pressure was specified at the inlet surface corresponding to a perfectly expanded exit Mach number. For the ambient region surrounding the nozzle flow, a characteristic boundary condition was defined, and the downstream static pressure was set equal to the ambient pressure. Adiabatic no-slip boundary condition was specified on all nozzle walls. The grid contained around 8 million points.

The code has been validated against mean velocity measurements under cold conditions.[38] Cold-flow comparisons for three-stream jets similar to the one discussed here have shown similar level of agreement.

2.1.2 LES

For the LES, The PARCAE solver discussed above was used in its unsteady implementation. The solver uses implicit backward three-layer second-order time integration with explicit five stage Runge-Kutta dual time stepping. The spatial discretization of the inviscid flux is based on the weighted averaged flux-difference splitting algorithm of Roe.[39,40] The viscous flux is discretized using a second-order central difference scheme. The time-evolving jet flow is simulated using a hybrid RANS/LES approach.[41] Near the wall region the Spalart-Allmaras turbulence model[42] is used to model the turbulent viscosity, while in the free shear flow the computation relies on the subtle dissipation of the upwind scheme, using the method proposed by Shur *et al.*[40]

The computational grid extended $60D_t$ in the axial direction and 20 D_t in the radial direction; it contained approximately 40 million elements. For each nozzle flow, it was imposed a perfectly expanded exit, with constant total pressure, total temperature, and zero flow angle. For the ambient region surrounding the nozzle flow, a non-reflecting characteristic boundary condition was imposed, and a buffer layer was implemented near the outflow. An adiabatic no-slip boundary condition was specified on the nozzle wall. The computation included the internal nozzle and external plume. Figure 2.3 shows the mesh used, as well as example vorticity and pressure contours of the computation.

For nozzle AXI04U, the LES results reported here represent 885 time steps of separation $\Delta t = 5 \times 10^{-6} s$. To improve the accuracy of the statistics, azimuthal averaging at six meridional planes at azimuthal angles $\phi = 0°$ to $300°$, separated by $60°$, was applied. This

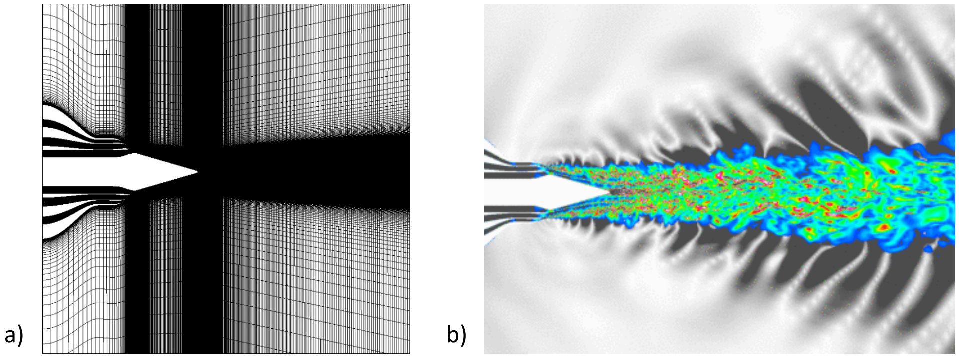

Figure 2.3: a) LES computational mesh; b) LES instantaneous fields, with inner region showing vorticity contours and outer region plotting the magnitude of the pressure fluctuation, $|p'/p_\infty| < 0.004$.

is justified by the fact that the azimuthal coherence at separation of 60° is very weak,[43] essentially making each meridional plane statistically independent.

For nozzle ECC09U, the LES results represent 2000 time steps of separation $\Delta t = 10 \times 10^{-6} s$. Only the planes of $\phi = 0°$ and $\phi = 180°$ have been used. Eccentricity made azimuthal averaging impossible for this case.

2.2 Comparison of Flow Fields

The first step for the comparison between LES and RANS results is the examination of flow fields computed with each technique. The magnitudes of main importance are mean axial velocity and Reynolds stress, the latter as calculated with equation 1.26.

2.2.1 Nozzle AXI04U

Figure 2.4 plots contours of the mean axial velocity normalized by the primary exit velocity $\overline{u}/U_p$ on the plane of symmetry for RANS and LES predictions. Both flow fields are very similar. LES predicts a faster spreading thus moderately smaller potential core: defining the potential core as the region where the maximum mean axial velocity is 90% or higher than the primary fully expanded velocity,

$$\overline{u}_{max,pot.core} \;\geq\; 0.9\; U_p \tag{2.1}$$

the potential core length predicted by LES extends up to $x/D_t \approx 1.7$, while the one predicted by RANS extends up to $x/D_t \approx 3.2$. It is also noted that the wake from the plug is accentuated in the RANS simulation. The LES provides a fairly reliable and averaged result for the mean velocity despite the relatively small number of time steps used. Figure 2.5 provides additional comparisons of normalized velocity along the axial centerline and transversely at one diameter downstream from the tip of the plug. It can be noted the faster spreading of the LES results towards the centerline of the jet: the flows mix sooner, creating a peak of velocity in the centerline around $x/D_t = 1.5$, upstream from the RANS predicted peak around $x/D_t = 3$. Fig. 2.5b shows a lower velocity gradient near the centerline and also lower peaks of velocity at the wake of the plug.

The analogous comparisons for the Reynolds stress are shown in Figs. 2.6 and 2.7. It is visible here that the LES results have insufficient number of time steps to construct reliable statistics for the entire domain. They have reached a fairly stable result for $x/D_t \leq 7$ that allows to draw conclusions from it, but become unreliable downstream. It should be noted that the contours for LES are averaged onto a half plane and then reflected to show the effect of the full jet. Within the region $x/D_t \leq 7$, the comparison between RANS and LES is very good in terms of levels and shapes of the distributions.

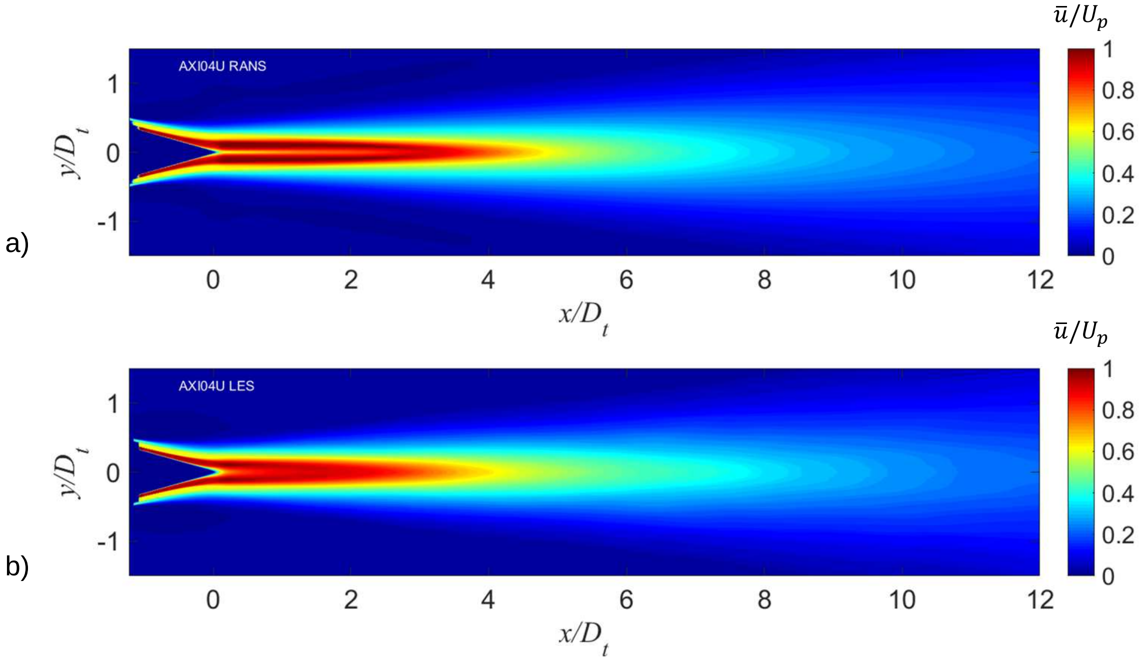

Figure 2.4: Contour plots of normalized mean axial velocity $\overline{u}/U_p$ of nozzle AXI04U. a) RANS and b) LES.

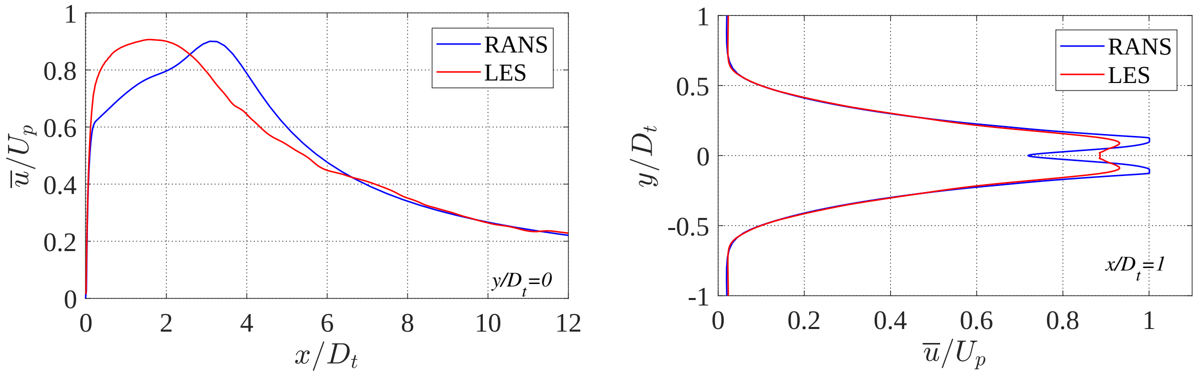

(a)

(b)

Figure 2.5: Plots of normalized velocity of nozzle AXI04U a) along centerline $y/D_j = 0$ and b) transversely at $x/D_j = 1.0$.

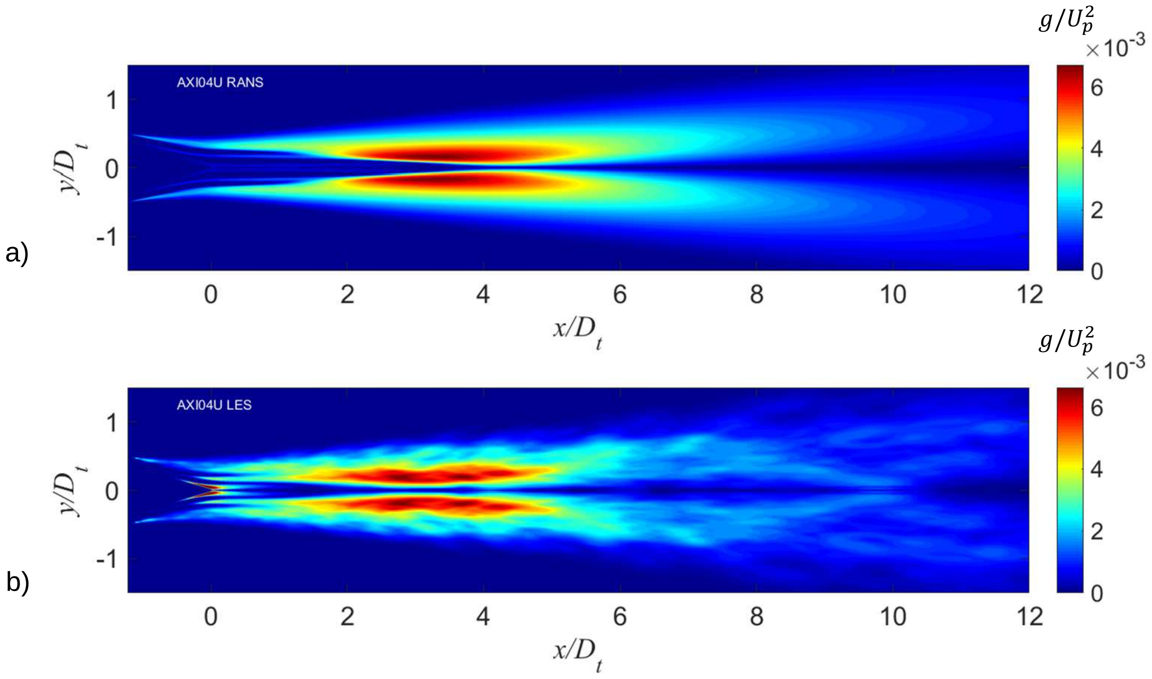

Figure 2.6: Contour plots of Reynolds stress g/U_p^2 of nozzle AXI04U. a)RANS and b)LES.

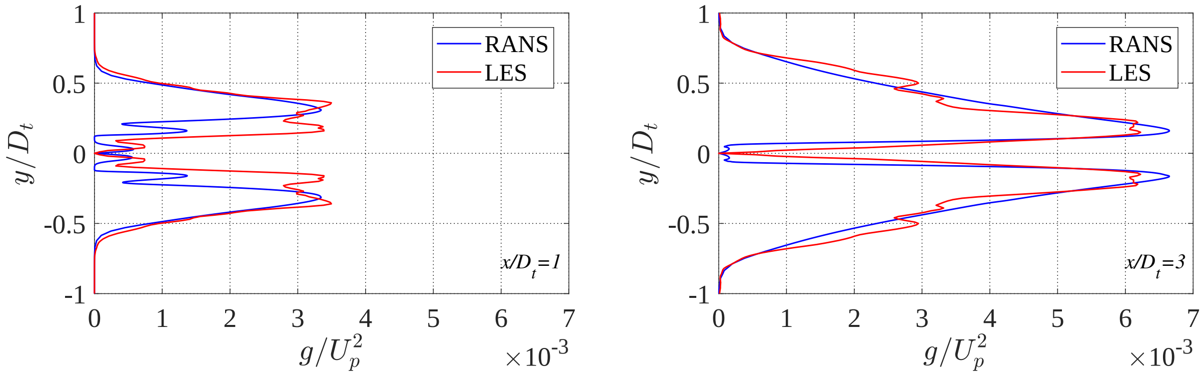

(a)

(b)

Figure 2.7: Plots of normalized Reynolds stress of nozzle AXI04U a) along $x/D_j = 1.0$ and b) along $x/D_j = 3.0$.

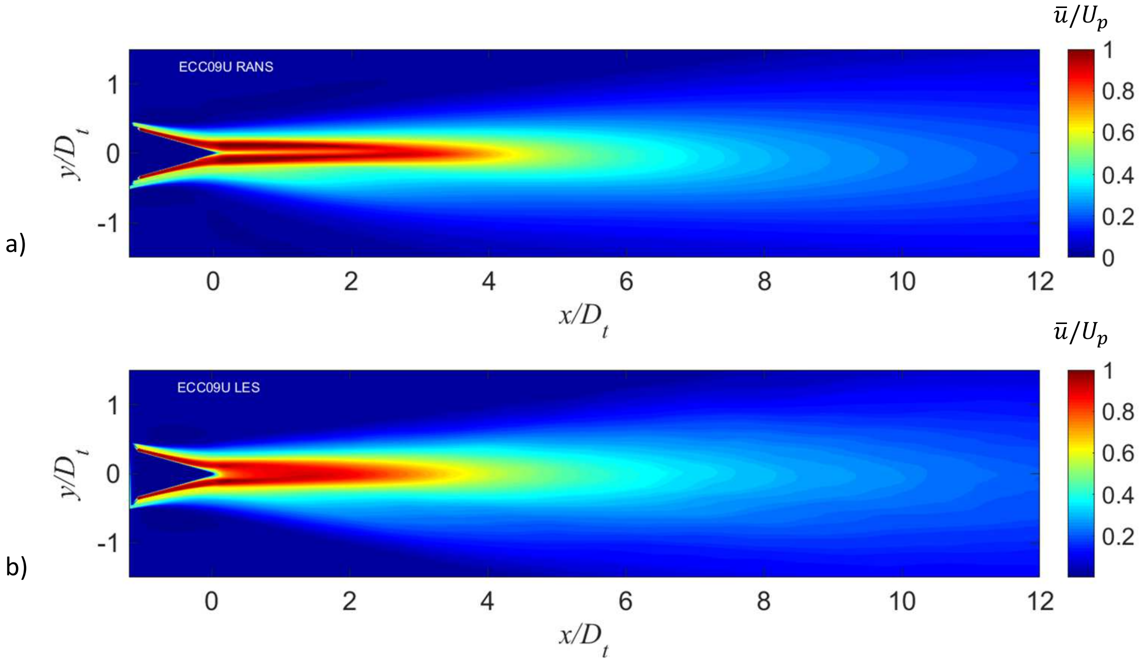

Figure 2.8: Contour plots of normalized mean axial velocity $\overline{u}/U_p$ of nozzle ECC09U. a) RANS and b) LES.

2.2.2 Nozzle ECC09U

Figures 2.8 and 2.9 plot the normalized mean axial velocity for the nozzle ECC09U. As in the axisymmetric case, it can be noted a faster spreading and smaller potential core in the LES than in the RANS. The potential core extends up to $x/D_t \approx 1.8$ in the LES and to $x/D_t \approx 3.0$ in RANS. The asymmetry produced by the eccentricity of the nozzle is evident: there is a significant concentration of low-speed flow on the underside of the primary jet. In general terms, RANS and LES predictions show a good level of similarity.

Figures 2.10 and 2.11 show the analogous comparisons for normalized Reynolds stress for nozzle ECC09U. Although the LES contour in Fig. 2.10 shows a distribution not fully converged to an averaged result, it is reasonably good taking into account that there is no azimuthal averaging for this case, only 2000 time steps for each plane. It is stable enough to

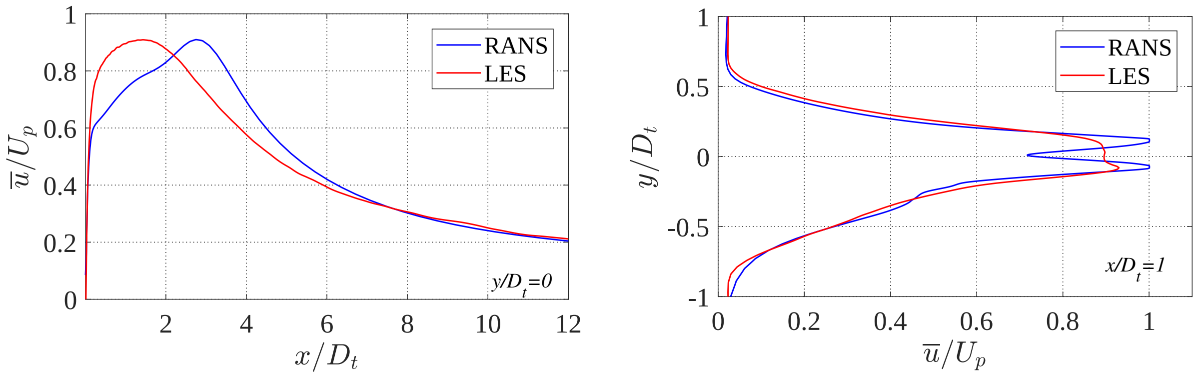

(a) (b)

Figure 2.9: Plots of normalized velocity of nozzle ECC09U a) along centerline $y/D_j = 0$ and b) transversely along $x/D_j = 1.0$.

draw conclusions for at least $x/D_j \leq 6$, and becomes unstable downstream. The comparisons between RANS and LES show good agreement in terms of levels and distributions.

The asymmetry caused by the eccentricity of the nozzle is very noticeable. The stronger presence the tertiary flow on the downwards direction greatly suppresses the high peak of Reynolds stress produced on $2.0 \leq x/D_t \leq 3.0$, having instead a slightly stronger outer shear layer, very visible on $0.0 \leq x/D_t \leq 2.0$. This can also be noted in Fig. 2.11a, where there is a higher peak on the upper part ($\phi = 180°$) and the lower part shows two maximums corresponding to the two different shear layers. Downstream, at $x/D_t = 3$, the outer shear layer vanishes as shown by Fig. 2.11b. The differences between RANS and LES results show that the region of highest g at $\phi = 180°$ predicted by LES is upstream from the RANS prediction, and that the values for g are in general higher for LES at the region $\phi = 0°$.

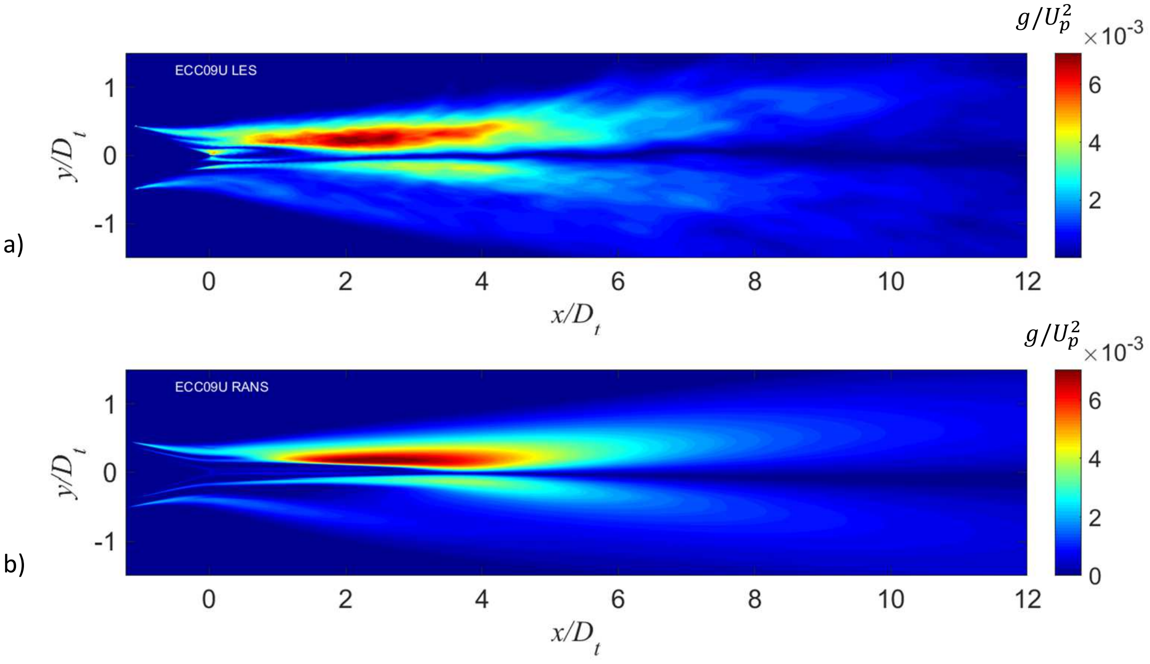

Figure 2.10: Contour plots of Reynolds stress g/U_p^2 of nozzle ECC09U. a)RANS and b)LES.

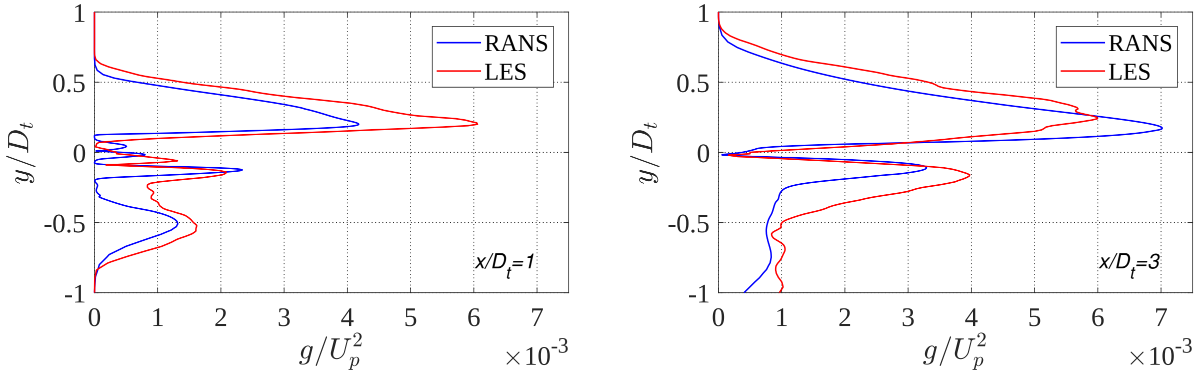

(a)

(b)

Figure 2.11: Plots of normalized Reynolds stress of nozzle ECC09U a) along $x/D_j = 1.0$ and b) along $x/D_j = 3.0$.

Chapter 3

Outer Surface of Peak Stress

In section 1.2.2 it was surmised that, in multi-stream jets, the turbulent eddies in direct contact with the ambient are the main noise generators. In a three-stream jet like those considered here, these eddies are initially in the tertiary (outer) shear layer, then progressively transition to the secondary and primary shear layers as the different flows mix. In RANS simulations, this is represented by the statistics on the outer-most peak of Reynolds stress g as explained in section 1.2.3. This results in the concept of the "outer surface of peak stress" (OSPS), where the convective velocity of the turbulent eddies is calculated with equation 1.27, repeated here for clarity:

$$U_c(x, r, \phi) \;=\; \overline{u}(x, y_{OSPS}(x, \phi), \phi) \tag{3.1}$$

In this section are presented the procedures and results of OSPS detection for RANS and LES results on nozzles AXI04U and ECC09U.

3.1 OSPS Based on RANS

For the location of the OSPS based on RANS results, the grid points are grouped axially into fine cross sections that will be treated as 2D, i.e. as if all the data of each cross section pertained to the same axial coordinate. Each cross section is then divided into azimuthal sections, typically of 2.5 degrees, from its centroid. This centroid is calculated as the geometrical center of the points of highest mean velocity (90% or more of the maximum mean axial velocity of the cross-section) as done by Papamoschou.[3] For each azimuthal sector, an initial point of search is set at a safe distance further from the centroid than the expected region of OSPS, but inside the jet in order to avoid noisy data. A good point for this is typically where the mean axial velocity decays to 33% of the maximum velocity of the cross section.

From the starting point, the properties of the flow are interpolated using inverse distance weighting, including the angle of velocity gradient ϕ_g. A new point is then created on the direction of that angle, at a distance δ very small in comparison to the flow cross section. This process is repeated for a certain number of steps, resulting in a "ray" of points that follows smoothly the gradient of mean velocity. This is shown schematically in Fig. 3.1. The reason why the search is performed following the velocity gradient instead of simply radially inwards is explained later.

The Reynolds stress g is one of the properties computed by interpolation on each point of the ray. The first maximum is located using the criterion that the function $max(g_j, g_{j-1})$ has M_{zero} consecutive zero slopes, that is, the value of g does not increase for M_{zero} points. The first point of this M_{zero} points is the point of g_{max}. This is illustrated in Fig. 3.2, where the coordinate η is used to denote the progression along a ray and which increases with the radial coordinate r. When the search along the interpolated points finds the peak value, it uses the nearest, non-interpolated point as the final point. This search along a ray is repeated

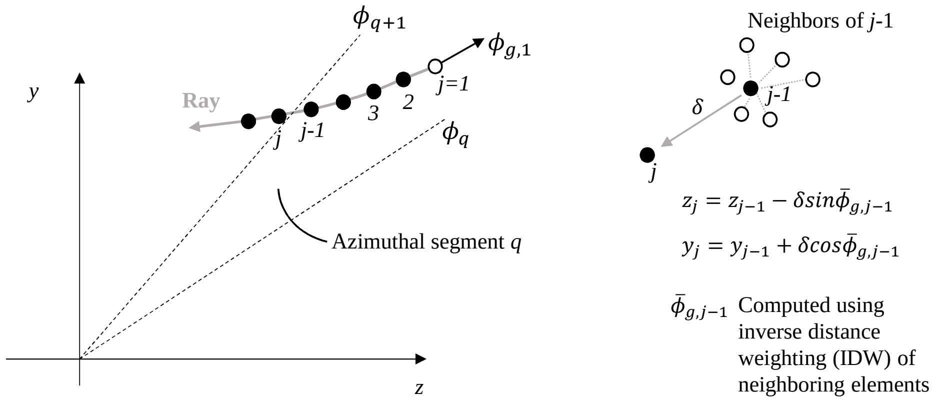

Figure 3.1: Schematic illustrations of ray generation for its OSPS detection.

for all azimuthal sections, and the peak points are interpolated on a regular surface. The final surface is found joining all cross sections of the jet, and a smoothing is applied along the azimuthal direction using Savitzky-Golay filtering.[44]

This same procedure was also done for the same purpose in Ref. 3. The outer point of peak stress g_{max} is found there searching radially along the azimuthal sections. That created unrealistic results in cases where the jet cross section was distorted and the g distribution had sharp azimuthal gradients. In these cases, a radial search loses physical sense because the jet is no longer axisymmetric.

Turbulence itself is caused by a velocity gradient, as expressed by the evolution equation for the turbulent kinetic energy for the simiplified case of homogeneous turbulence[31]

$$\frac{Dk}{Dt} = -\overline{\mathbf{u}'\mathbf{u}'} : \nabla\bar{\mathbf{u}} - \epsilon \tag{3.2}$$

where D/Dt means the total derivative associated with the mean flow and ϵ is the dissipation. The main component of Reynolds stress g is also calculated using the mean axial velocity gradient. If one wants to find the locus of peak Reynolds stress, following the mean axial

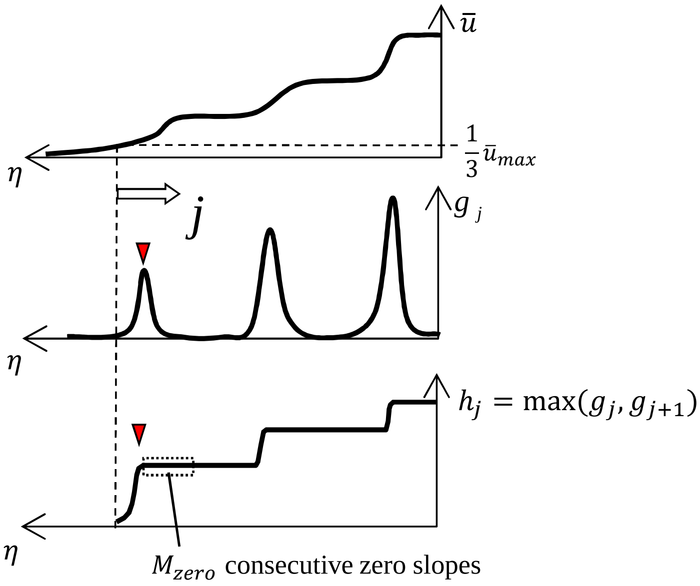

Figure 3.2: Schematic illustrations of the OSPS search based on RANS along a ray, from Papamoschou.[3]

velocity gradient on the cross section instead of radially searching is more consistent with the theory. Although no difference is be expected on the analysis of an axisymmetric jet, there can be a noticeable improvement for the case of eccentric jets. The comparison between the two methods is shown at example sections in Fig. 3.3.

Once the OSPS has been detected, the convective velocity U_c is modeled as the mean axial velocity on that surface, following Eq. 3.1. Figure 3.4 plots three-dimensional views of the OSPS of jets AXI04U and ECC09U obtained using the rays (following mean axial velocity gradient) method. The OSPS experiences a sudden convergence where the outer streams become totally mixed with the primary shear layer. This is followed by a gradual convergence near the end of the primary potential core, downstream of which the OSPS diverges slowly. Nozzle ECC09U shows a big elongation of the low-speed region on the downwards side, a result of the thickening of the tertiary flow. The convergence of the shear layers into one actually never happens in that region. Instead, the outer shear layer diverges until it vanishes

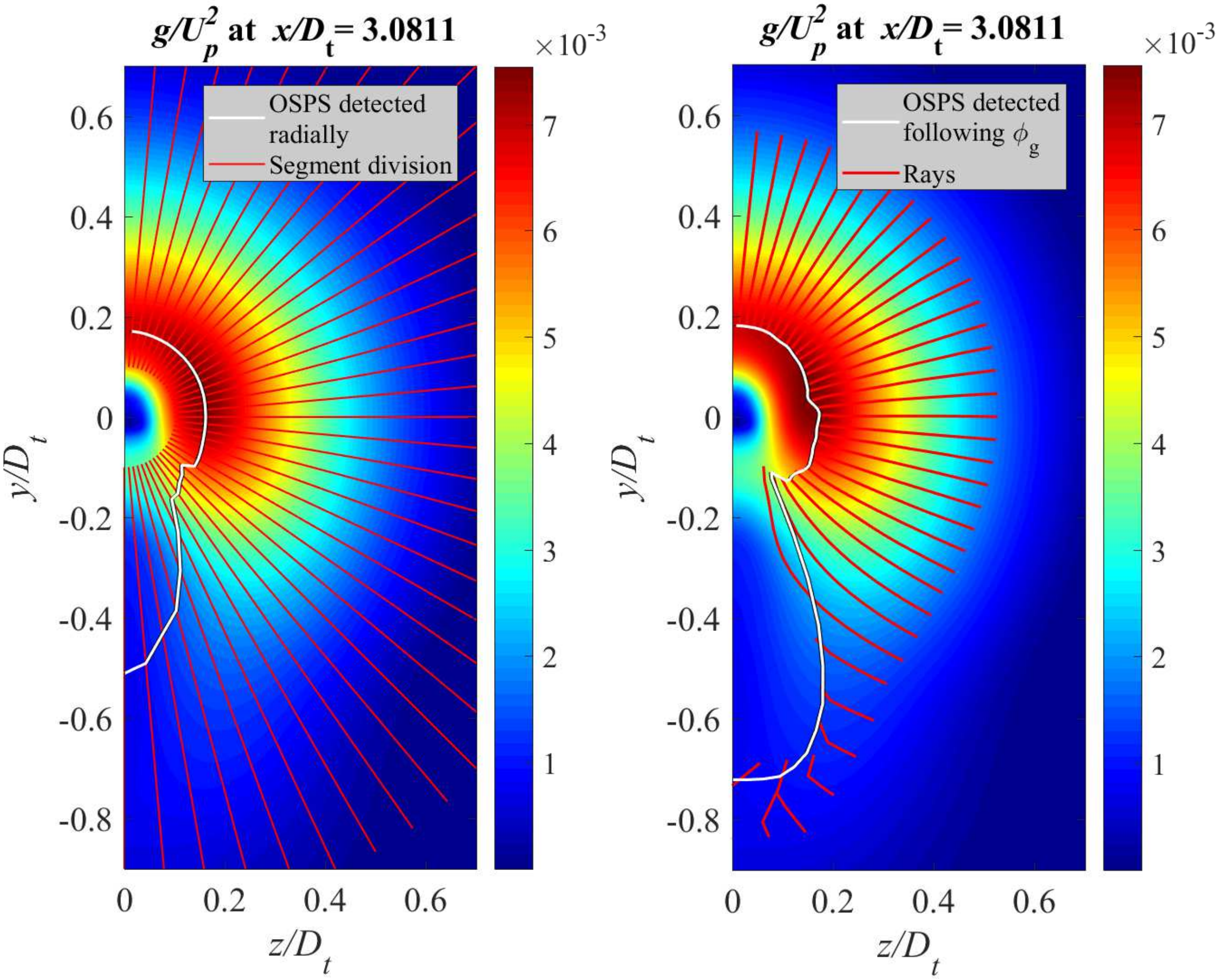

(a) (b)

Figure 3.3: Contours of RANS-based Reynolds stress and OSPS (white line) at $x/D_t = 3.1$ obtained by a) radial search within segments and b) search along rays.

due to spreading and dissipation. At that point it stops representing a local maximum of Reynolds stress g anymore. Therefore, the OSPS “collapses” on the primary shear layer. The “fin” created by the outer shear layer before vanishing is also visible in Fig. 3.3b.

The location of the OSPS on the outer shear layer, together with the fact that it spreads to a region of lower velocity around the downwards direction, causes a significant reduction in the convective velocity U_c and convective Mach M_c distributions. This is key to the reduction in the noise generated towards directions near $\phi = 0°$ seen in Ref. 33.

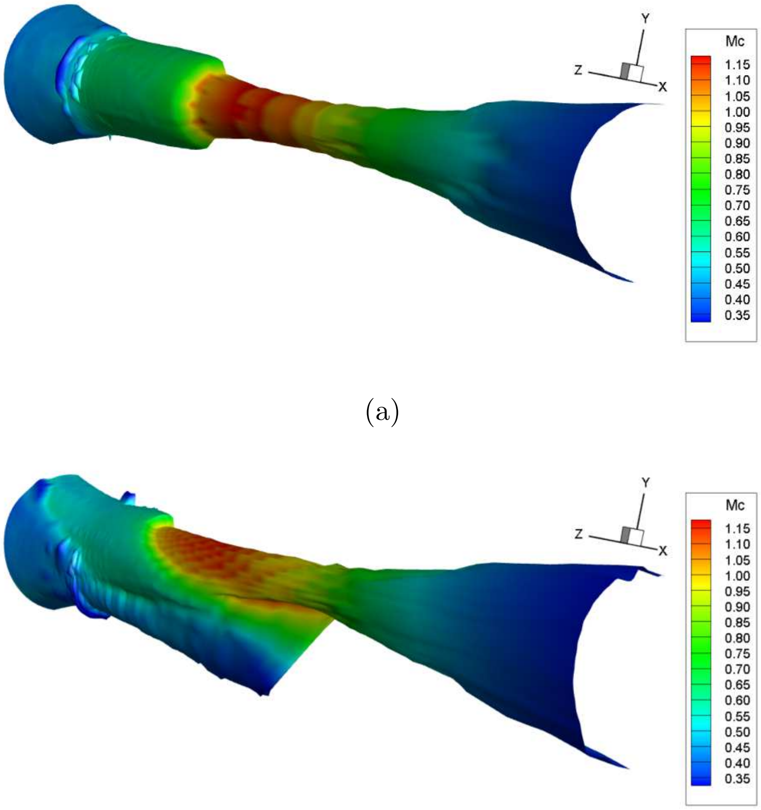

(a)

(b)

Figure 3.4: M_c distribution on RANS-based OSPS surfaces. a) Nozzle AXI04U and b) Nozzle ECC09U.

3.2 OSPS based on LES

The detection for the OSPS in LES is similar as in RANS. The difference relies on the LES data being in azimuthal planes rather than in a whole 3D domain, so the search is performed radially. This is valid for all azimuthal planes of nozzle AXI04U, but only for the symmetry plane of ECC09U. In addition, because of the inherent noise of the LES results, the detection scheme for this case has to be treated very carefully. For the nozzle AXI04U, there are 6 azimuthal planes with notable noisy data in them. For consistency, the OSPS is located on each one and the convective velocity is computed along each OSPS following the procedure outlined in section 3.3. The final result is the average of all six distributions of peak stress locations and convective velocities.

On the other hand, data of nozzle ECC09U is only available along the symmetry plane and eccentricity makes azimuthal averaging impossible. Fortunately, the bigger amount of time steps (2000) of this simulation allowed for better averaged, less noisy results. The final results for nozzle ECC09U are directly the OSPS and convective velocity for each plane, slightly smoothed in the axial direction by Savitzky-Golay filtering.[44]

Figure 3.5 shows the OSPS location over the Reynolds stress contours for both nozzles, which will be discussed in section 3.4.

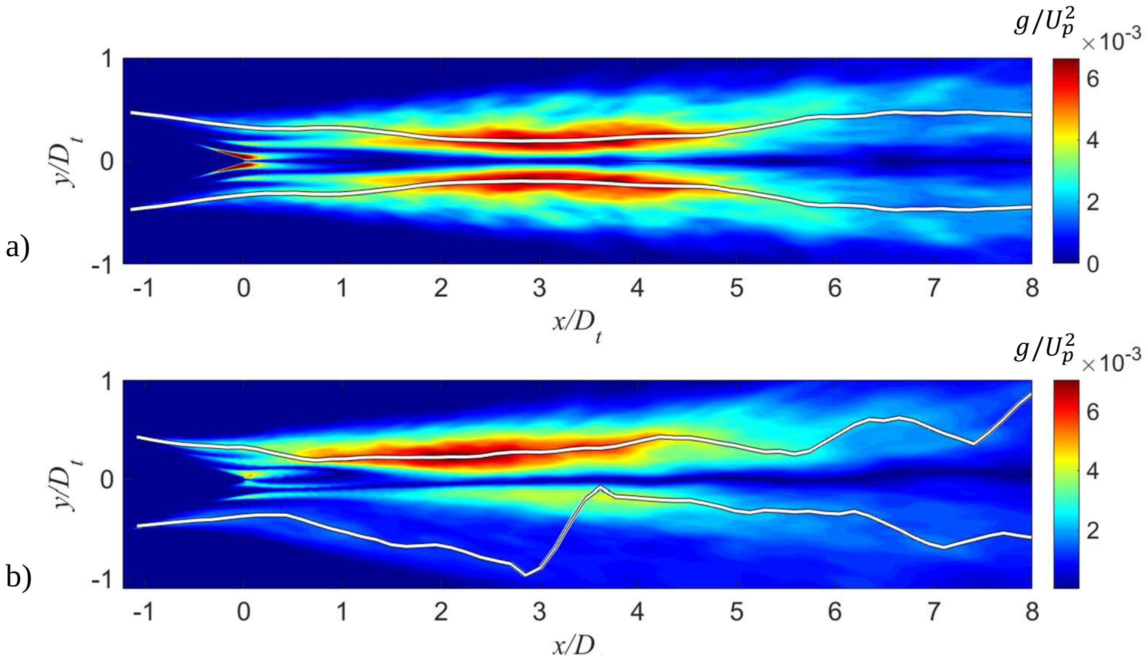

Figure 3.5: OSPS location (white line) over normalized Reynolds stress contours. a) Nozzle AXI04U and b) ECC09U.

3.3 Space-time correlation of LES data

The LES solution allows calculation of the space-time correlation anywhere within the computational domain. For a given azimuthal angle, the axial space-time correlation of the axial velocity fluctuation u', in normalized form, is

$$R_{uu}(x,r;\xi,\tau) \;=\; \frac{< u'(x,r,t)u'(x+\xi,r,t+\tau) >}{u'_{rms}(x,r)u'_{rms}(x+\xi,r)} \tag{3.3}$$

where rms denotes the root mean square; ξ is the axial separation to the central point, i.e. where the convective velocity is being calculated; and τ is the time delay applied to the signal of position $x+\xi$. A simple explanation for this procedure is that R_{uu} is the measure of similarity between two u' signals separated ξ in space and τ in time. Given a simple curve of space-time correlation, the convective velocity at a certain point is the axial

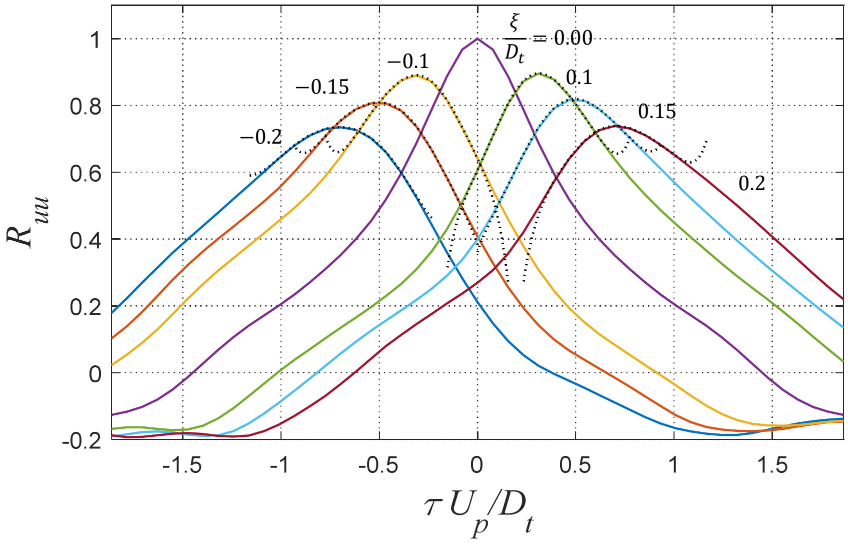

Figure 3.6: Space-time correlation R_{uu} on the OSPS at $x/D_t = 1.0$ for nozzle AXI04U. Dashed lines indicate fits by seventh-order polynomials to accurately detect the peak of each correlation.

separation divided by the delay of its maximum value. A similar formulation is used for R_{pp}, the space-time correlation of p'. Examples of space-time correlations are plotted in Fig. 3.6.

Computation of the convective velocity at a given point of the computational grid involved space-time correlations at small axial separations around this point, with minimum correlation of 0.4. Because each correlation function comprises a discrete set of points, to accurately locate the maximum value of the correlation at axial separation ξ_i a seventh-order polynomial was fitted around the peak of the correlation curve (dashed lines in Fig. 3.6). The time separation τ_i corresponding to the maximum value of the polynomial (i.e., the root of the derivative) was then calculated using a Newton-Raphson iteration method. The convective velocity for this axial separation is $U_{c,i} = \xi_i/\tau_i$ and the overall U_c at point (x, r) was obtained by averaging $U_{c,i}$ over the separations that satisfied $R_{uu_{max}} > 0.4$.

A limiting factor for space-time correlations is the decaying rate of R_{uu} with axial separation. This is related to the "life" of the turbulent structures traveling downstream: the distance they travel while appearing and disappearing. In order to satisfy $R_{uu_{max}} > 0.4$, the distance between the two points of a measure must be lower for high decay rates, also called short length scales; and higher for low decay rates, called long length scales. It is seen that the length scales of the space-time correlations are shorter at the beginning of the jet and grow downstream, as shown in Fig 3.7.

Figure 3.7 illustrates the need for shorter separations in early regions of the flow, with the maximum of Fig. 3.7b being $\xi/D_t = 0.15$. Measures downstream such as in Fig. 3.7e show that values of $\xi/D_t = 0.3$ still maintain high peaks, meaning a long correlation length scale. This means that the separation values used depend on the jet flow, and should be "calibrated" when surveying different flows.

When surveying a region of very small length scale, the axial separation ξ needed can require time separation on the order of a few time steps. This gives a time τ between maximums that is inaccurate because of the limited time samples. This was a problem solved with polynomial fitting for the nozzle AXI04U. However, in nozzle ECC09U, its large time step (10 µs) also results in an unrealistic shape of the correlations: they look spiked, with only very few points of high R_{uu}. An example for this case is shown in Fig. 3.8, where the posterior calculation of U_c loses accuracy. Nevertheless, this only happens in certain areas of short length scales and high convective velocities, and its effects are expected to be mitigated by polynomial fitting.

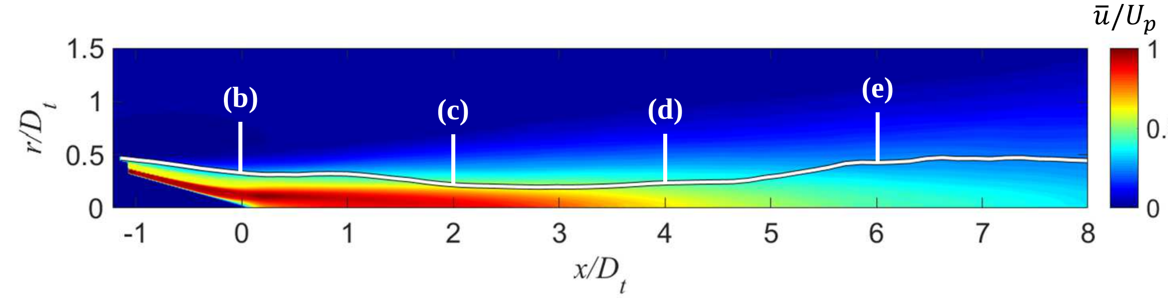

(a) Contour of mean axial velocity for nozzle AXI04U. White line: OSPS.

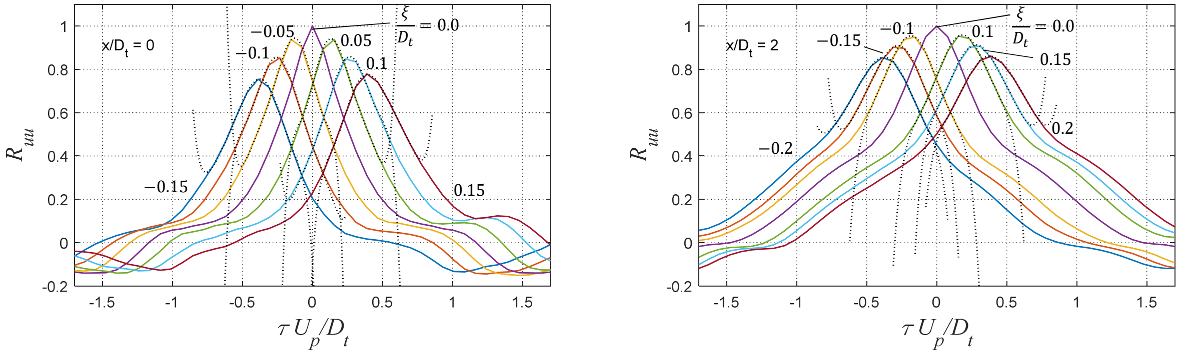

(b) $x/D_t = 0.0$

(c) $x/D_t = 2.0$

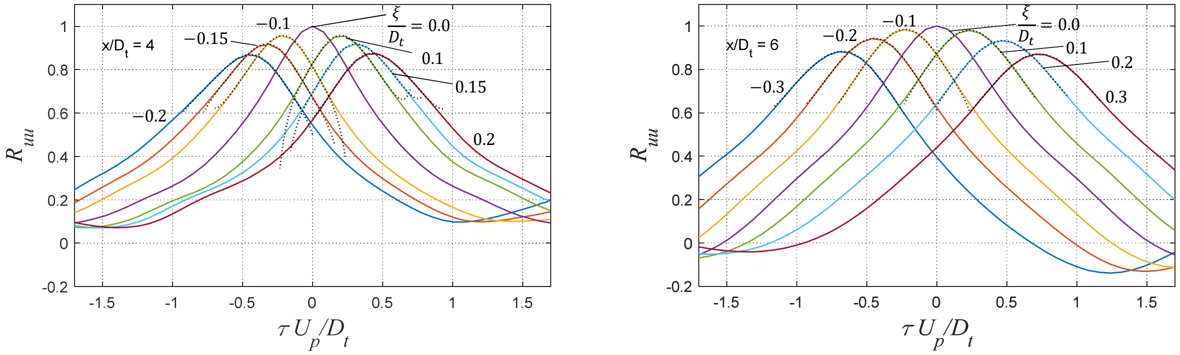

(d) $x/D_t = 4.0$

(e) $x/D_t = 6.0$

Figure 3.7: OSPS over mean axial velocity contour of nozzle AXI04U, with examples of space-time correlations along its path.

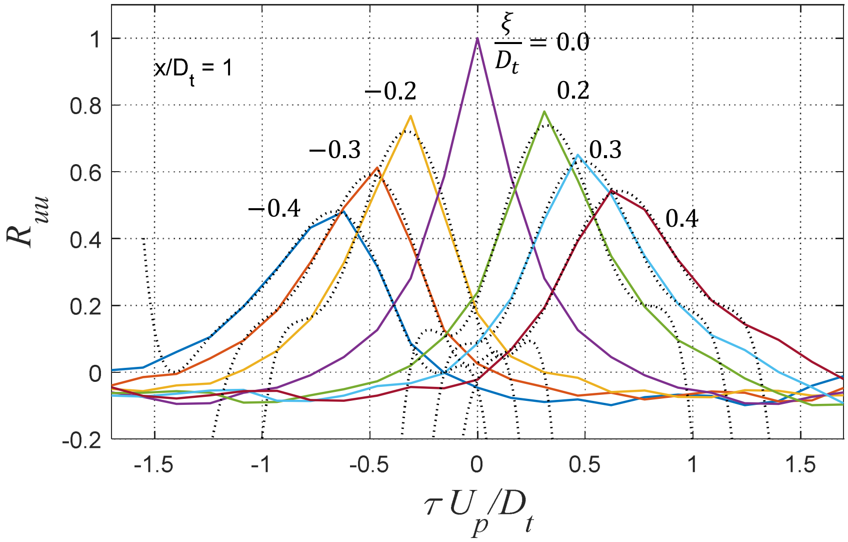

Figure 3.8: Space-time correlation R_{uu} on the OSPS at $x/D_t = 1.0$ for nozzle ECC09U.

3.4 Comparison of RANS and LES Results

Once the OSPS location and its corresponding U_c distribution are determined for the RANS and LES methods discussed, the next step is to compare them. The following subsections address this process, first on nozzle AXI04U and then for nozzle ECC09U.

3.4.1 Nozzle AXI04U

Figure 3.9 plots the radial coordinates of the OSPS for RANS and LES. The two surfaces are practically identical up to $x/D_t = 2$, with the plot showing clearly the inward transition of the OSPS from the tertiary to the secondary to the primary shear layer. For $2 \leq x/D_t \leq 7$, the two surfaces are close but the LES result is shifted outward, reflecting the more rapid spreading of the LES jet. As discussed earlier in section 2.2, Reynolds stress results for $x/D_t > 7$ are unreliable because of the limited number of samples.

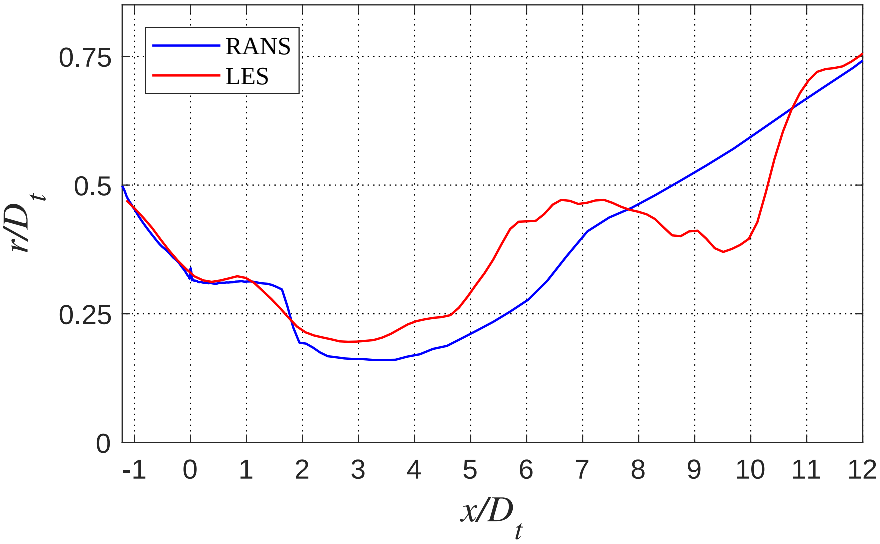

Figure 3.9: OSPS distribution for RANS and LES, nozzle AXI04U.

The comparison of convective velocities on the OSPS is seen in Fig. 3.10. The RANS- and LES-based trends are similar and show the increase in U_c as the most energetic eddies move from the tertiary (low speed) to the secondary (medium speed) to the primary (high speed) shear layer, followed by a decline in U_c as the mean velocity decays past the end of the primary potential core. There are moderate quantitative differences between the RANS and LES results, with RANS predicting a peak value of U_c that is about 10% higher than that predicted by LES.

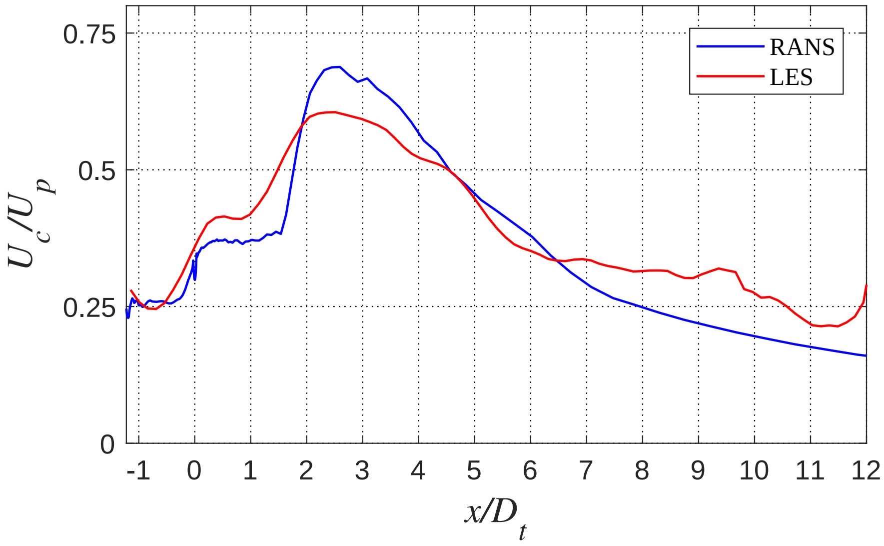

Figure 3.10: U_c distribution for RANS and LES along their respective OSPS, nozzle AXI04U.

3.4.2 Nozzle ECC09U

Because of the eccentricity of nozzle ECC09U, the comparison of OSPS location is different between the two available planes, $\phi = 0°$ and $\phi = 180°$. The result for the first angle is shown in Fig. 3.11. There is a good similarity in terms of trends, and a reasonable one in values. The inwards movement of the shear layer is elongated for the LES, followed by a slightly faster spreading. There is a clear "collapse" for both curves around $x/D_t = 3$, where the outer shear layer vanishes. At that point, the peak radius of the LES-based OSPS is $r/D_t = 0.97$, 26% more than the RANS-based OSPS peak of $r/D_t = 0.77$. After the inwards transition, the curves show good similarity up to $x/D_t = 6$, where the LES-based OSPS loses accuracy due to a lack of averaging.

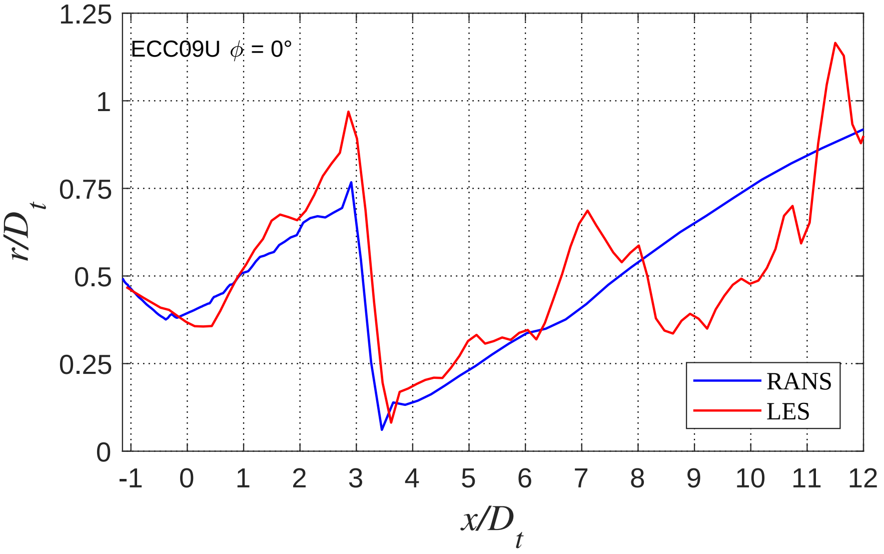

Figure 3.11: OSPS distribution for RANS and LES and angle $\phi = 0$, nozzle ECC09U.

Figure 3.12 shows the comparison of convective velocities obtained by RANS and LES. The two curves are very similar and clearly show a slightly decaying U_c where the OSPS is placed on the outer shear layer. Around $x/D_t = 3$, the collapse of the OSPS to the primary shear layer causes the convective velocity to rise suddenly. The difference in peak values is around 17% of the RANS-based peak.

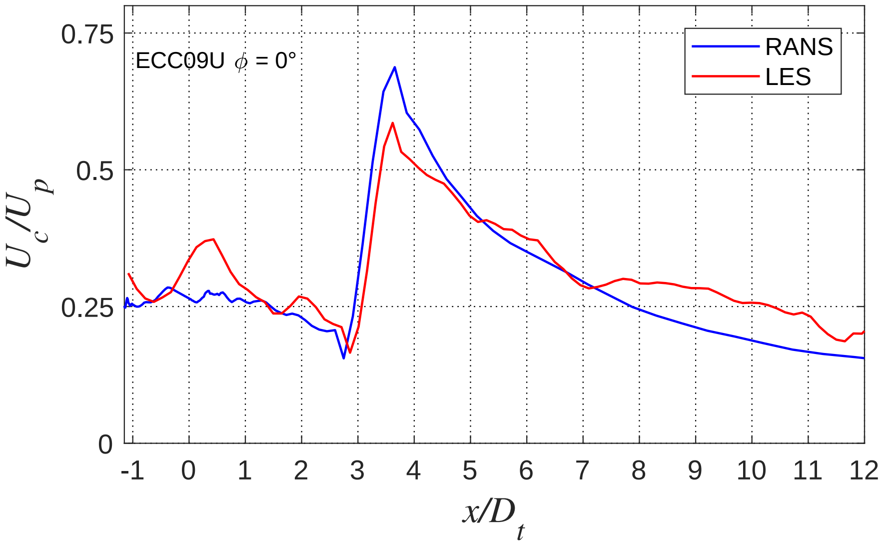

Figure 3.12: U_c distribution for RANS and LES along their respective OSPS, for $\phi = 0$ nozzle ECC09U.

Figure 3.13 shows the OSPS location for angle $\phi = 180°$. Again, the curves show similar features in terms of trends, with an overall faster spreading of the LES predictions. Because the tertiary stream is deflected, the OSPS follows the secondary shear layer, which is quickly merged with the primary. This transition happens around $x/D_t = 0.75$ for RANS, and around $x/D_t = 0.5$ for LES. In the latter case, the collapse of the OSPS is smoothed due to a more aggressive use of Savitzky-Golay filtering.

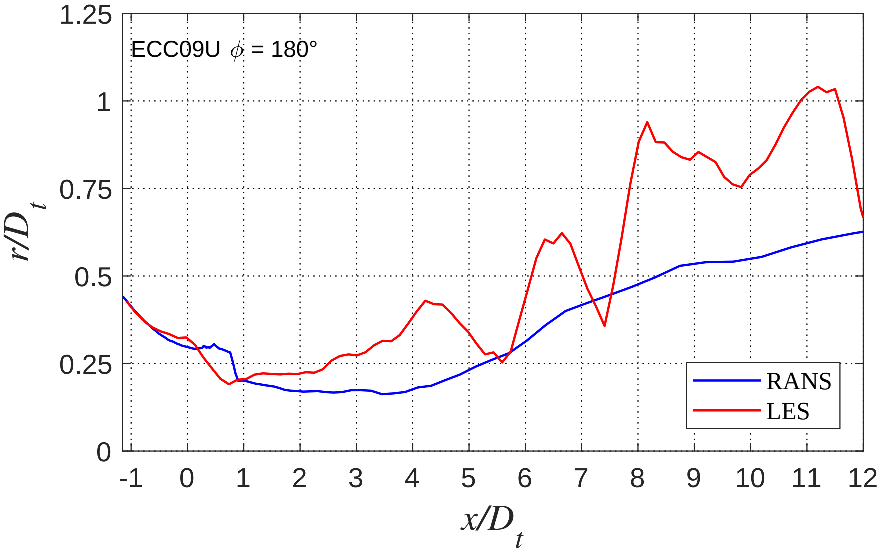

Figure 3.13: OSPS distribution for RANS and LES and angle $\phi = 180$, nozzle ECC09U.

The corresponding comparison between convective velocities for the angle $\phi = 180°$ is shown in Fig. 3.14. Because the comparison of OSPS locations is less agreeing than those of nozzle AXI04U and $\phi = 0°$ of nozzle ECC09U, it is reasonable to expect also less agreement for their convective velocities. However, the RANS- and LES-based trends are still similar. Similarly to nozzle AXI04U, there is a stepped increment in the convective velocity as the shear layers mix. However, because the tertiary flow is deflected such that there are only primary and secondary flows, only one sudden rise is seen in this case. Because of the difference in this transition seen in the OSPS, LES predicts such jump in velocity upstream from the RANS prediction. After that, the lower LES-based U_c is explained by a the faster spreading of its OSPS.

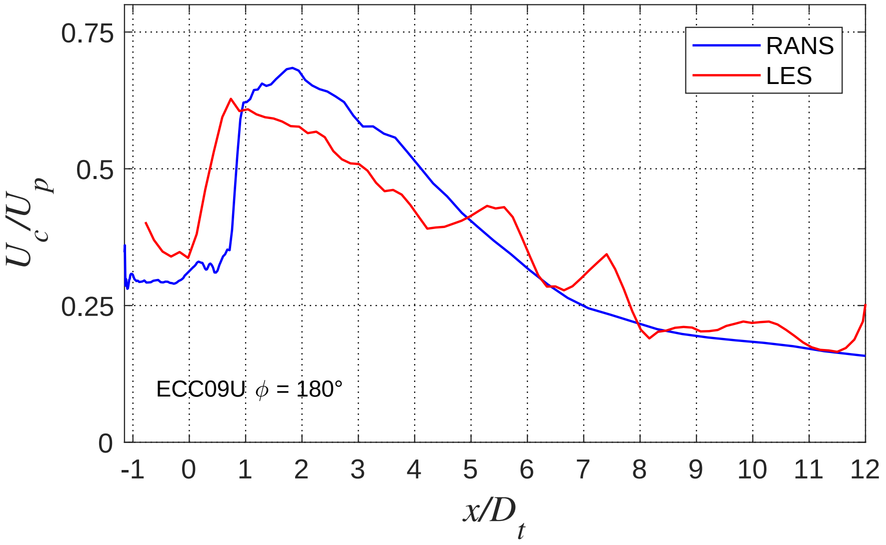

Figure 3.14: U_c distribution for RANS and LES along their respective OSPS, for $\phi = 180$ nozzle ECC09U.

Overall, all comparisons provide encouragement that the RANS flow field can yield a fairly accurate convective velocity distribution for the purposes of jet noise modeling.

Chapter 4

Radiator Surface

The radiator surface is a concept introduced in earlier studies of single- and dual-stream jets[27,43] and explained in section 1.2.3. It is defined as the closest surface to the jet centerline on and outside of which the propagation of pressure perturbation is governed by the homogeneous linear wave equation. It is on this surface that a linear model for jet noise, in the form of wavepackets, could be informed by turbulent statistics computed by low-cost methods such as RANS. One of the most important elements of a surface source model is the convective velocity U_c.

The criterion for the location of the radiator surface followed by Papamoschou *et al.*[27] is given by Eq. 1.22 and repeated here for convenience:

$$\frac{|\partial\overline{u}/\partial r|(x,\phi,r_{edge}(x))}{|\partial\overline{u}/\partial r|_{max}(x,\phi)} \;=\; \kappa \tag{4.1}$$

The usual threshold κ is selected to be $\kappa = 0.01$, and for a multi-stream jet, one may select $|\partial\overline{u}/\partial r|_{max}(x)$ to be the outermost peak of the mean velocity gradient, similar to the definition of the OSPS.

There are several challenges with this definition of radiator surface. Accurate measurement of the mean velocity gradient at the edge of the jet is very difficult experimentally as the results can be quite noisy; the threshold κ in Eq. 4.1 is somewhat arbitrary and the placement of the radiator surface could be sensitive on its selection; and, for multi-stream jets, the proper gradient in the denominator of Eq. 4.1 is not clear. In the following sections, the location using the definition of Eq. 4.1 and its validity are discussed. Alternative definitions are contemplated, although a definitive practical definition remains a target for future efforts.

4.1 Location of Radiator Surface

The location of the radiator surface is computed using the same kind of algorithm used for the detection of the OSPS, explained in section 3.1. In order to find the outermost peak of $|\partial\overline{u}/\partial r|$, the search process starts from outside the flow and moves towards the center following the 2D gradient of mean axial velocity. Once found, the search goes in reverse to locate the edge of the jet using the threshold set by Eq. 4.1.

4.1.1 Reference Peak of Velocity Gradient

The choice of defining $|\partial\overline{u}/\partial r|_{max}(x)$ in Eq. 4.1 as the outermost peak, instead of the absolute peak, stems from the assumption that the outer shear layer dominates sound production. However, from a practical standpoint, use of the absolute maximum of $|\partial\overline{u}/\partial r|$ may be more convenient. Figure 4.1 plots the results of the two definitions for nozzle AXI04U. There are slight differences of the two surfaces up to $x/D_t = 1.5$, beyond which they coincide as the outer shear layers vanish. The small difference upstream is explained by the fact that the profile of mean velocity at the first stages of the flow is very steep. Therefore, the velocity gradient decreases so fast outside the flow that it reaches both threshold values almost at

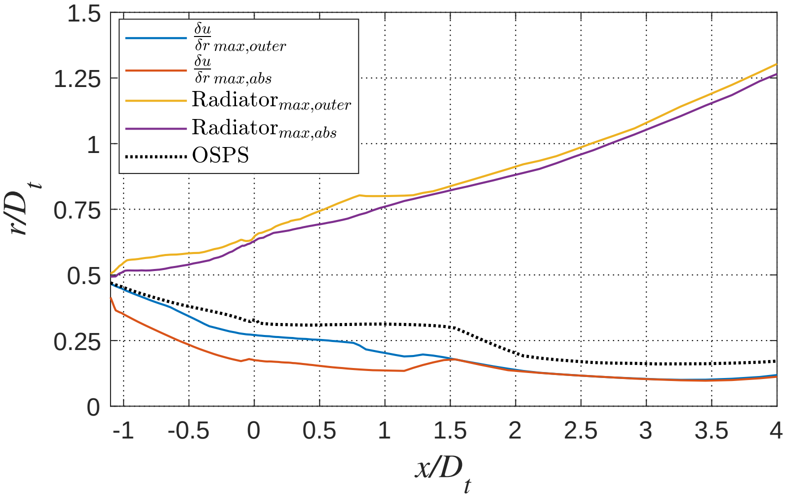

Figure 4.1: Comparison of radiator and related surfaces, using the outermost or absolute peak of $|\partial\overline{u}/\partial r|$ for nozzle AXI04U.

the same position. It is also interesting to note that the OSPS "collapse", at the end of the outer shear layers, begins at the union of the curves of peak $|\partial\overline{u}/\partial r|$.

The same analysis gives a very similar result for nozzle ECC09U at azimuthal angle $\phi = 180°$: the layers of maximum gradient of velocity quickly unify so there is no difference between the two possible radiator surfaces. It is even more intuitive in this case, as for this region there are only two flows. However, there is a certain disparity for angle $\phi = 0°$, where the outer shear layer grows notably before vanishing. This is seen in Fig. 4.2. There is a visible drop in the radius of the outermost peak gradient that matches very well the OSPS. Up to that point, outermost and absolute peaks of gradient of velocity are clearly distinguishable. This translates into a faster growth of the radiator surface based on the outer peak. Nevertheless, this difference does not grow more than half a diameter, and disappears after the collapse of the outermost shear layer. Given that this angle $\phi = 0°$ is expected to be the region of maximum distance between surfaces, it can be said that the difference between using one or other peak is overall small. For the sake of consistency with the physics of the problem, the radiator surfaces calculated by Eq. 4.1 for the following sections take as a reference the outermost peak of mean velocity gradient.

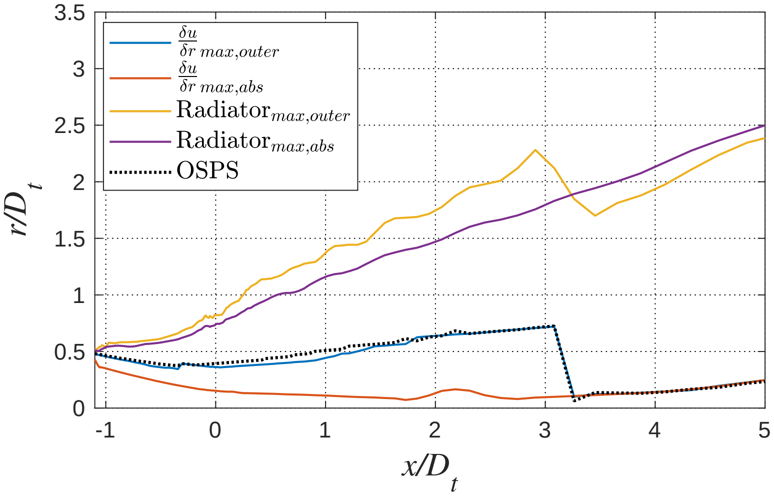

Figure 4.2: Comparison of radiator and related surfaces, using the outermost or absolute peak of $|\partial\overline{u}/\partial r|$ for nozzle ECC09U at $\phi = 0$.

4.1.2 Sensitivity to Threshold Value

One of the concerns of using the definition of Eq. 4.1 is that the threshold value κ is arbitrary. It exists as the conversion of an analytical limit to a real, measurable condition, therefore the only constraint it needs to comply is to be small. However, there are other values of κ other than $\kappa = 0.01$ that are also small, and the resulting radiator surface may be different between them. To test this, the radiator surface of each nozzle have been located using different threshold values: 0.005, 0.01, 0.015, 0.02 and 0.03. Figure 4.3 shows the result for AXI04U. It is evident that all of the possible radiator surfaces have similar trends. They differ in values, although the maximum difference is no much more than 0.25 diameters.

Also, variations in low values of κ result in more different radiator surfaces than variations in higher values.

Figure 4.4 plots the corresponding surfaces for nozzle ECC09U, where similar behavior can be seen. In this case, the surface obtained with $\kappa = 0.005$ presents a particularly strange behavior, product of the difficulties of calculations with such small values of velocity gradient.

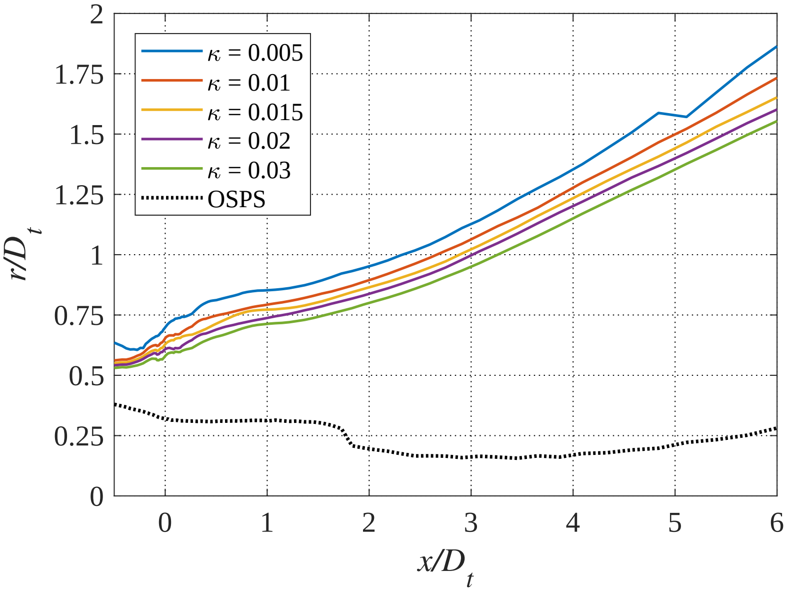

Figure 4.3: Comparison of radiator surfaces obtained with different threshold value κ, nozzle AXI04U.

From this analysis, it can be concluded that there is a consistent difference between the resulting radiator surfaces of different threshold values κ, but they have very similar trends. Smaller values of κ would be theoretically more precise but they present more difficulties in their radiator surface location that may lead to a less accurate surface. Nevertheless, the possibility of using a different threshold value should be remembered in the following sections.

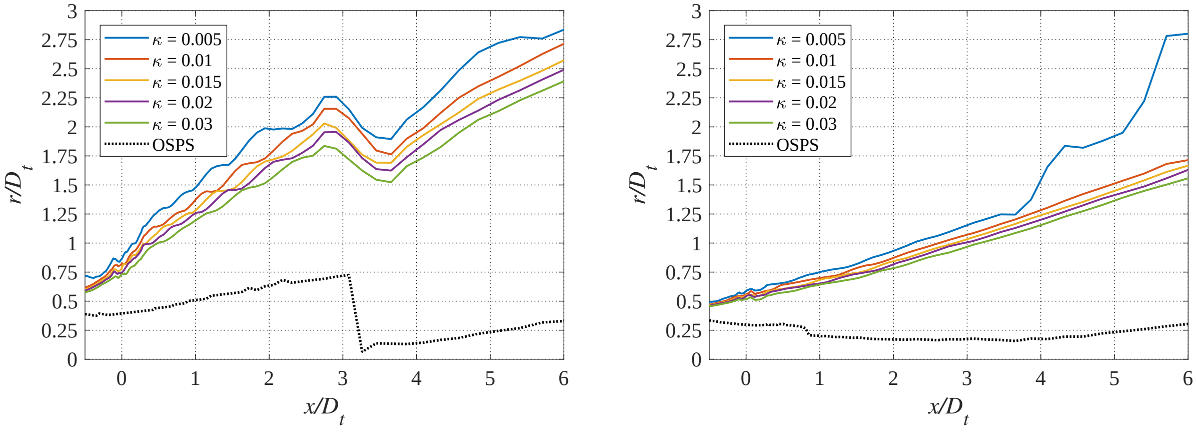

(a) $\phi = 0$ (b) $\phi = 180$

Figure 4.4: Comparison of radiator surfaces obtained with different threshold value κ, nozzle ECC09U.

4.2 Distribution of Convective Velocity

It is desired to find a connection between the convective velocity distributions on the OSPS and on the edge of the jet. To this end, it is relevant to plot contours of U_c/U_p on the $x - r$ plane for nozzle AXI04U and nozzle ECC09U at $\phi = 0°$ and $\phi = 180°$, shown in Figs. 4.5, 4.6, 4.7, respectively. For all three figures, contour (a) shows U_c based on the space-time correlation of u' (R_{uu}), and contour (b) is based on the space-time correlation of p' (R_{pp}). The former is relevant inside the vortical field, where the turbulent structures affect the velocity of the flow directly. The latter makes more sense when analyzing the outer flow, around the edge of the jet, where we seek the pressure imprint of the vortical eddies. The two distributions are similar, with an important distinction that will be discussed in the following. At a given axial location, U_c has a radial trend whereby it decreases outside the OSPS (depicted as red line), reaches a minimum, then rises sharply. The sharp rise is associated with the transition from the hydrodynamic to the acoustic field and the fact that acoustic disturbances can travel at large angles to the jet axis. This transition is faster in the case of the R_{pp}-based U_c. The overall trends are similar to those noted in a single-stream jet.[27]

The RANS-based radiator surfaces, as defined by the criterion of Eq. 4.1 with $\kappa = 0.01$ (dashed black line), fall marginally within the acoustic field for the R_{uu}-based distribution in Figs. 4.5a and 4.6a. On the contrary, it follows the transition layer quite accurately in Fig. 4.7a. This is where nozzle ECC09U has its tertiary stream depleted, and its flow resembles that of a two-stream flow. This result suggests that the definition of Eq. 4.1 loses validity in three-stream flows, but in dual- and single-stream jets it may describe well the transition given by correlations based on u'.

Figures 4.5b, 4.6b, and 4.7b show that RANS-based radiator surfaces fall well inside the acoustic field for all R_{pp}-based distributions. Therefore, they are too far outside the (pressure-based) edge of the jet to properly satisfy their intended role. A consequence of this is that the convective velocity on the radiator surface, as defined by Eq. 4.1, does not match the convective velocity on the OSPS.

The reverse question is now posed: What is the shape of the surface, near the edge of the jet, where the U_c distribution matches that on the OSPS? The result is the white lines in Figs. 4.5, 4.6 and 4.7; which for brevity are designated as "U_c match". They appear to track perfectly the hydrodynamic-acoustic transition of the R_{pp}-based U_c map, but are well inside the hydrodynamic region of the R_{uu}-based U_c map. The smoothness of the U_c-match lines, and their proximity to the hydrodynamic/acoustic boundary in the R_{pp}-based U_c, suggest that the U_c information on the OSPS is transmitted to the jet rotational/irrotational boundary as determined by space-time correlations based on p'. This provides encouragement that there is a surface, having the desired properties of the radiator surface, on which the RANS-derived convective velocity (on the OSPS) would inform the definition of the partial fields.

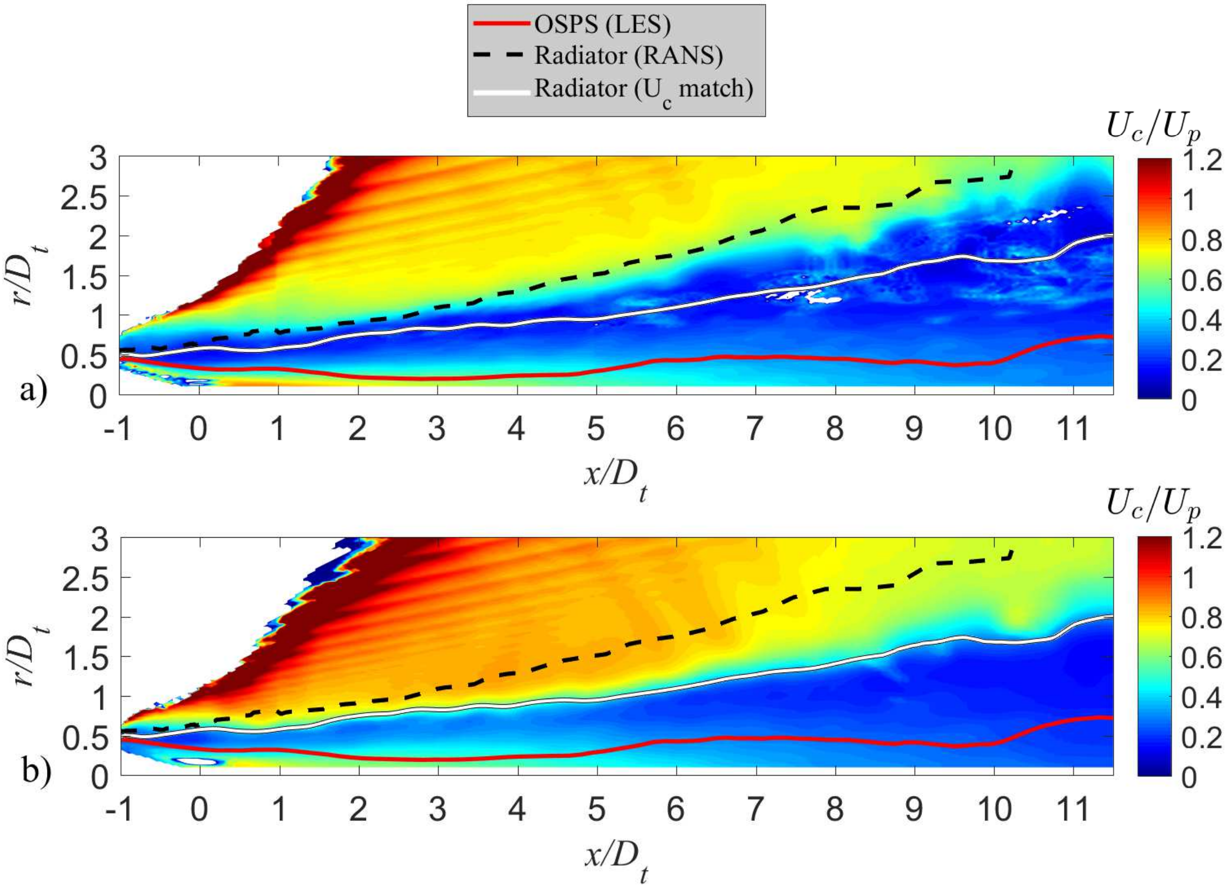

Figure 4.5: Distribution of normalized convective velocity U_c/U_p in nozzle AXI04U as determined by space-time correlations a) based on u' and b) based on p'. Red line: OSPS surface based on LES; black dashed line: classic definition of radiator surface; white line: radiator surface based on U_c-match criterion.

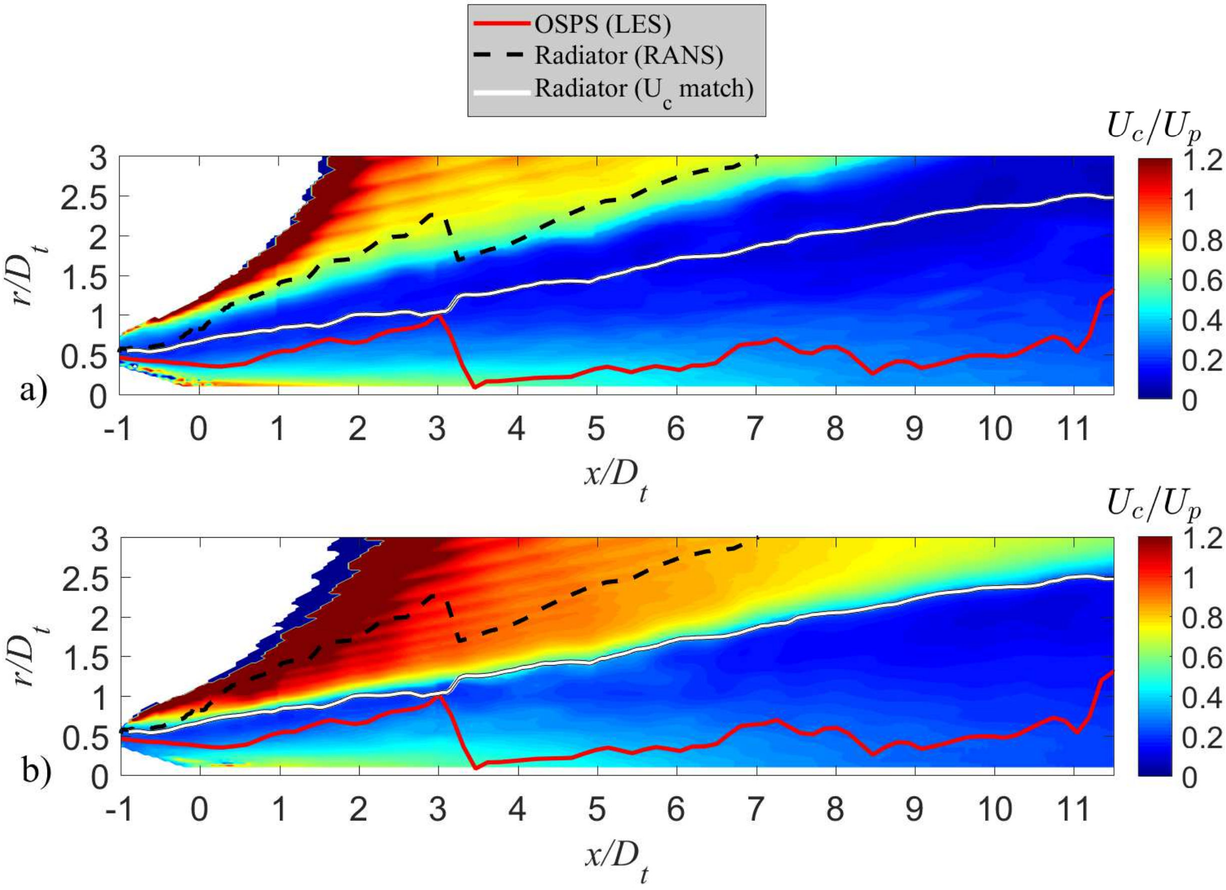

Figure 4.6: Distribution of normalized convective velocity U_c/U_p in nozzle ECC09U, $\phi = 0°$, as determined by space-time correlations a) based on u' and b) based on p'.

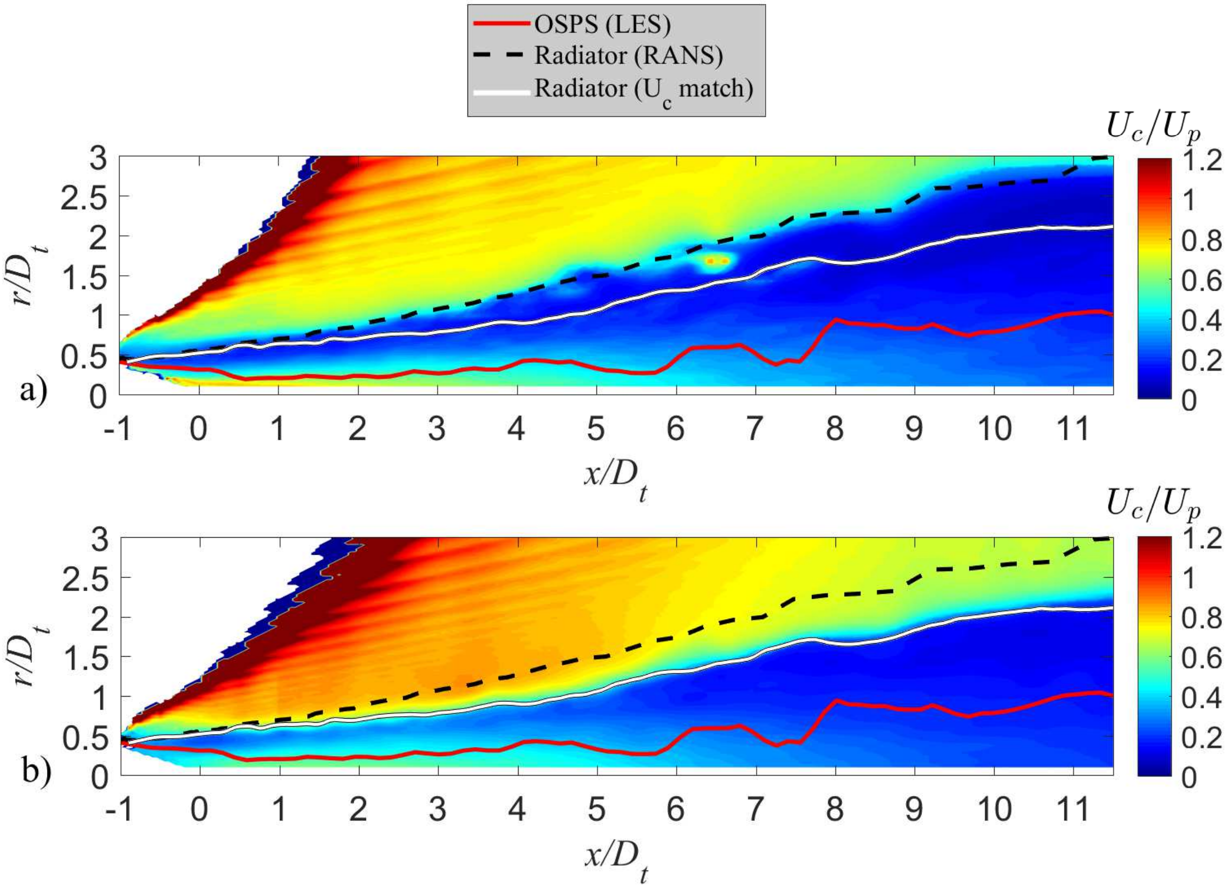

Figure 4.7: Distribution of normalized convective velocity U_c/U_p in nozzle ECC09U, $\phi = 180°$, as determined by space-time correlations a) based on u' and b) based on p'.

4.3 Distribution of Skewness of Pressure Field

An intriguing finding of earlier studies of Papamoschou *et al.* on the near pressure field of cold single- and dual-stream jets is the presence of a negative layer of skewness of p' near the edge of the jet.[43] Defining the normalized skewness as

$$Sk = \frac{< p'^3 >}{< p'^2 >^{3/2}} \tag{4.2}$$

the earlier studies found the radiator surface, as defined by Eq. 4.1 (with $\kappa = 0.01$), was practically coincident with the locus of $Sk \approx -0.3$. It is then interesting to examine whether similar trends hold in the case of hot three-stream jets.

Figures 4.8 and 4.9 present contour maps of the pressure skewness distribution on the $x - r$ plane for nozzles AXI04U and ECC09U, respectively. For each contour map, there is definitely a negative skewness layer near the edge of the jet. The radiator surface, as determined by the U_c match criterion discussed above (white line), appears to track the outer band of the negative skewness layer. On the other hand, the radiator surface as computed by the conventional means (dashed black line) is located well outside the negative skewness layer.

There are some additional features of interest in the skewness maps of Figs. 4.8 and 4.9. In the acoustic fields, there are positive values of skewness that suggest Mach wave radiation.[45] Inside the jet, the OSPS surfaces seem to follow a layer of zero or slightly positive skewness. This is more visible in Fig 4.9a, where two areas of zero skewness resemble the two shear layers present: the OSPS follows the outer one, until it collapses to the inner one.

Figure 4.10 plots the axial distribution of Sk along the three obtained U_c-match radiators. The values are consistently negative. It is believed that the trends are noisy because of the relatively small number of steps in the LES computation. The overall value of Sk along the radiator surface is lower than the previously proposed criterion of $Sk \approx -0.3$, and does not

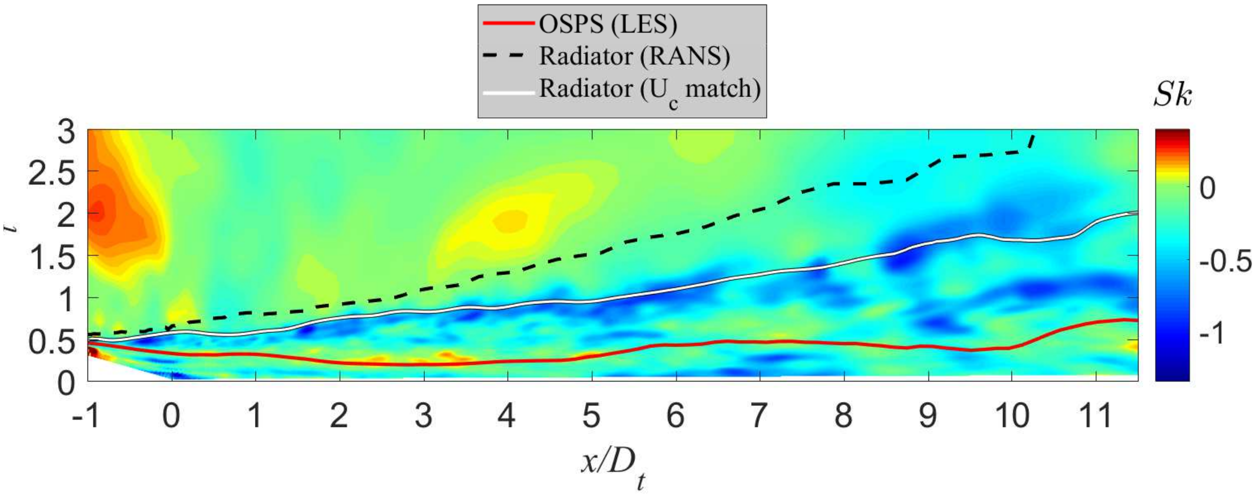

Figure 4.8: Distribution of normalized skewness of pressure field of nozzle AXI04U. Red line: OSPS surface based on LES; black dashed line: classic definition of radiator surface; white line: radiator surface based on U_c-match criterion.

appear to be constant along the surfaces. Nevertheless, these results, in combination with the findings of the previous studies, indicate that the negative skewness layer is an important feature of the pressure field that deserves further study.

The values of the skewness layer followed by the U_c-match lines seen in Fig. 4.9 are unusually low, particularly for $\phi = 180°$. Such values mean that there are strong negative events followed by less intense positive ones. The timewise evolution of p' at two locations on the symmetry plane of jet ECC09U is shown in Fig. 4.11. Figure 4.11a plots p' at a point with $Sk = -0.927$ in the direction $\phi = 0°$. As expected, the trace is marked by negative events much stronger than positive events. Figure 4.11b plots p' at a point located near the minimum skewness, $Sk = -1.66$, if the direction $\phi = 180°$. Few sudden, very strong negative events are evident in the plot, which are the reason for the very negative skewness. The physical cause of these sudden expansions is not understood and will be the topic of future investigations.

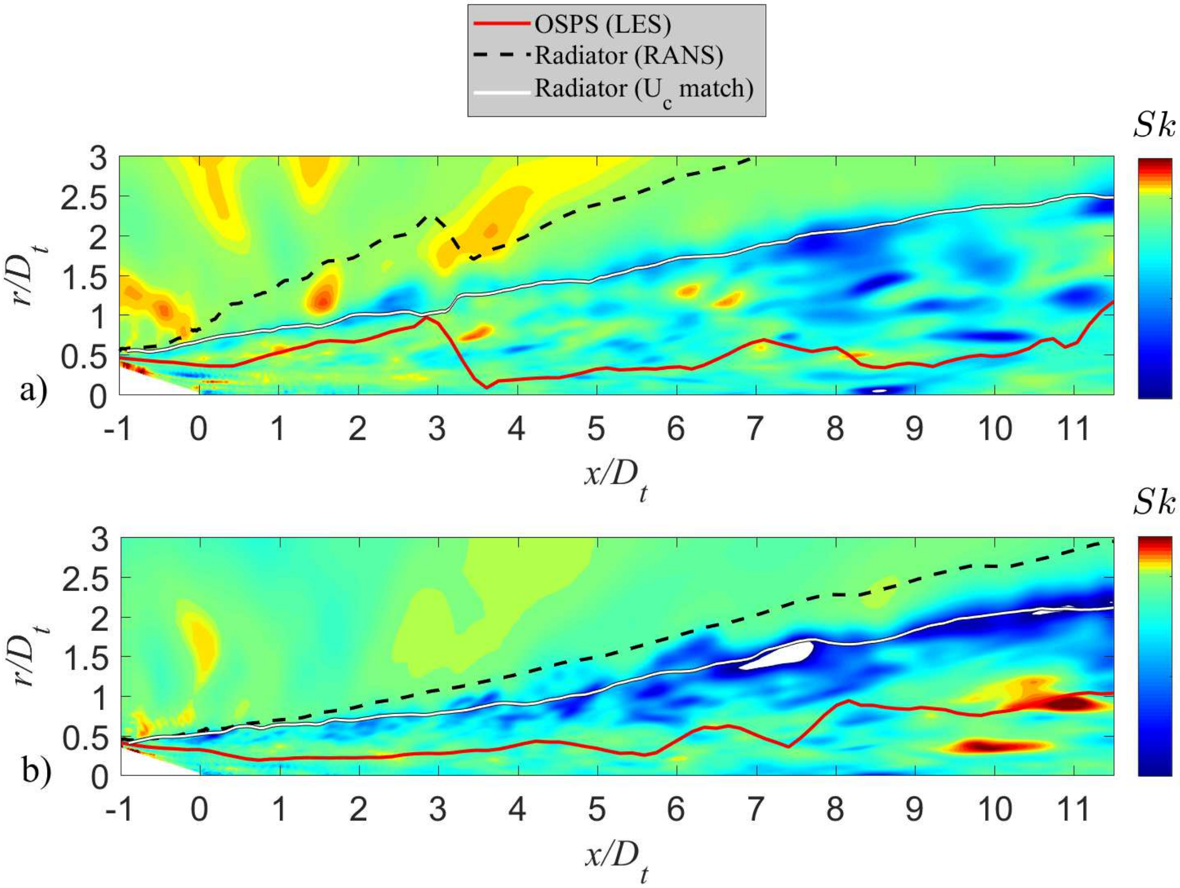

Figure 4.9: Distribution of normalized skewness of pressure field of nozzle ECC09U. a) $\phi = 0°$ and b) $\phi = 180°$.

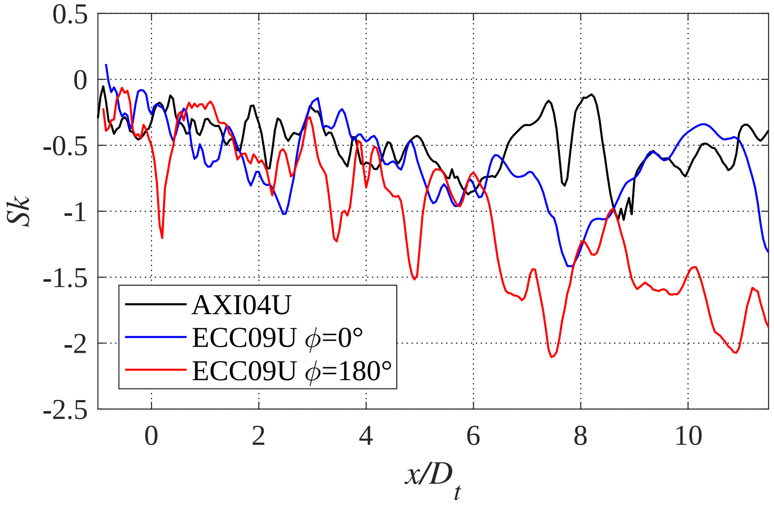

Figure 4.10: Distribution of Sk along radiator surfaces based on U_c-match criterion.

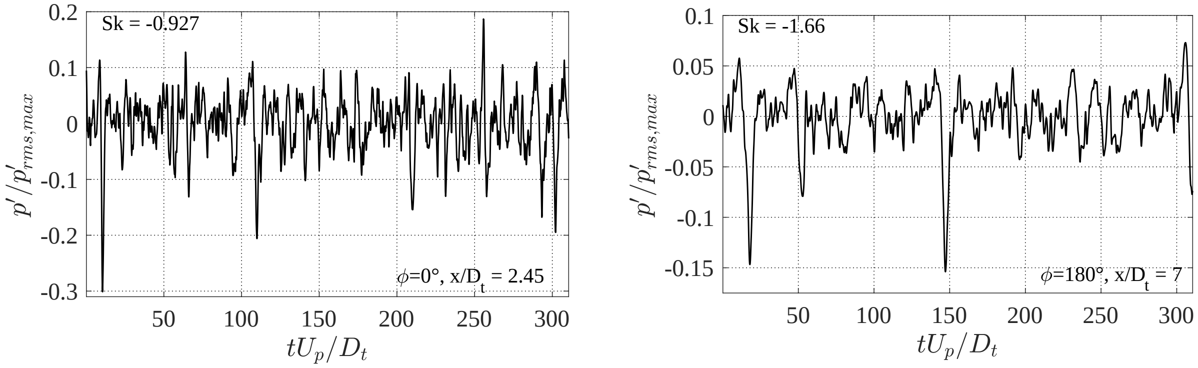

(a) $\phi = 0, x/D_t = 2.45$

(b) $\phi = 180, x/D_t = 7$

Figure 4.11: p' traces at the U_c-match surface

4.4 Distribution of Instantaneous Pressure Fluctuation

Given that the ultimate goal of this effort is prediction of acoustic radiation, it is interesting to visualize "raw" LES results and examine how the various surfaces defined here (OSPS, radiator) may fit with these results. Specifically, we wish to visualize the magnitude of the instantaneous pressure fluctuation p' on the cross-sectional plane $\phi = 0°$ throughout the domains of interest. Because of the large dynamic range of p', it is convenient to present the results in the logarithmic form

$$\ln\left(\frac{|p'|}{p'_{rms,max}}\right)$$

where $p'_{rms,max}$ is the maximum rms pressure fluctuation in each domain. The related contour maps are presented in Figs. 4.12 and 4.13, where the limits correspond to the range $10^{-4} \leq |p'|/p'_{rms,max} \leq 1$. Overlayed on the maps are the coordinates of the OSPS and radiator surfaces based on the U_c match criterion.

For the result of nozzle AXI04U in Fig. 4.12, the surfaces displayed were computed by time averaging on the plane $\phi = 0°$ only (encompassing the half planes $\phi = 0°$ and $\phi = 180°$). Inside the jet, the most energetic pressure events appear to line up with the OSPS, indicating the value of this surface in jet noise modeling. Outside the radiator surface, we observe a clear pattern of Mach waves radiating at the polar angle of peak emission which for this jet is around 30° relative to the jet axis.

The result of nozzle ECC09U is shown in Fig. 4.13. There is a clear asymmetry due to the geometry of the nozzle. The upper part of the jet ($y/D_t > 0$), corresponding to $\phi = 180°$, shows a behavior similar to AXI04U, with a pattern of Mach waves radiating near the angle of peak emission and the most energetic events aligned with the OSPS. On the lower part of the jet, however, the Mach wave emission is visibly reduced. The OSPS is located on the outer part of the region of energetic events until it collapses to the inner region.

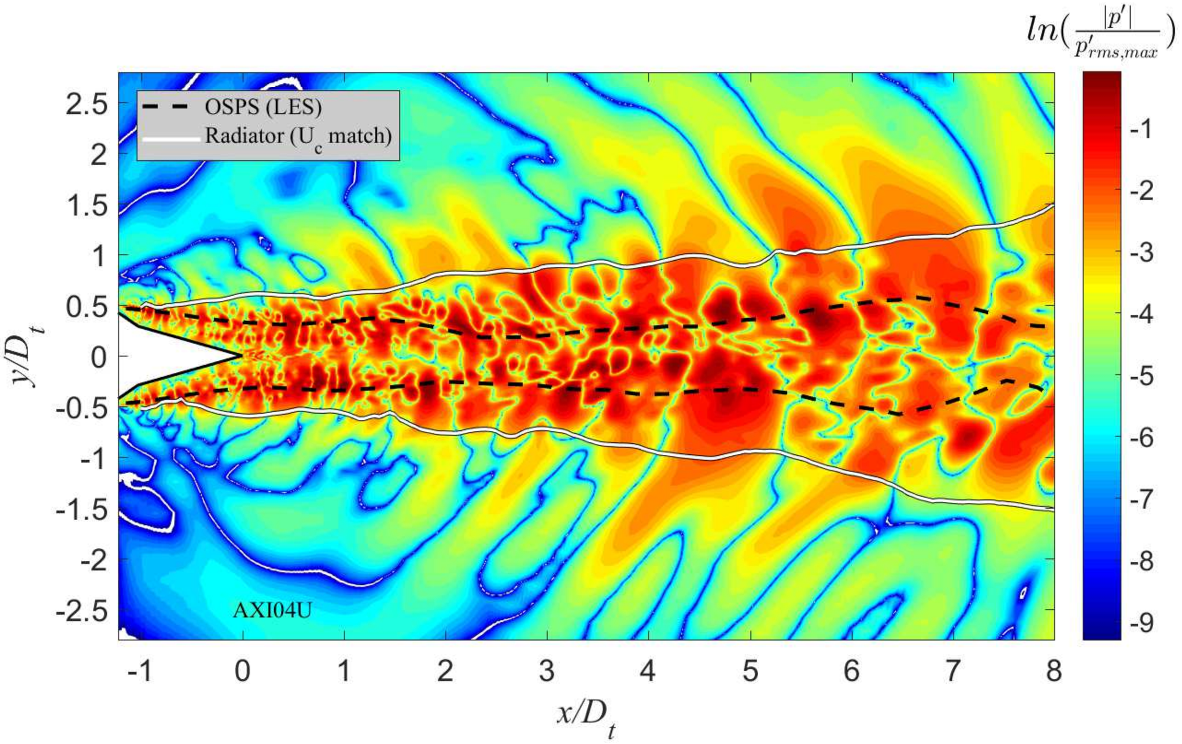

Figure 4.12: Distribution of the magnitude of the instantaneous pressure fluctuation of nozzle AXI04U, presented in normalized logarithmic form.

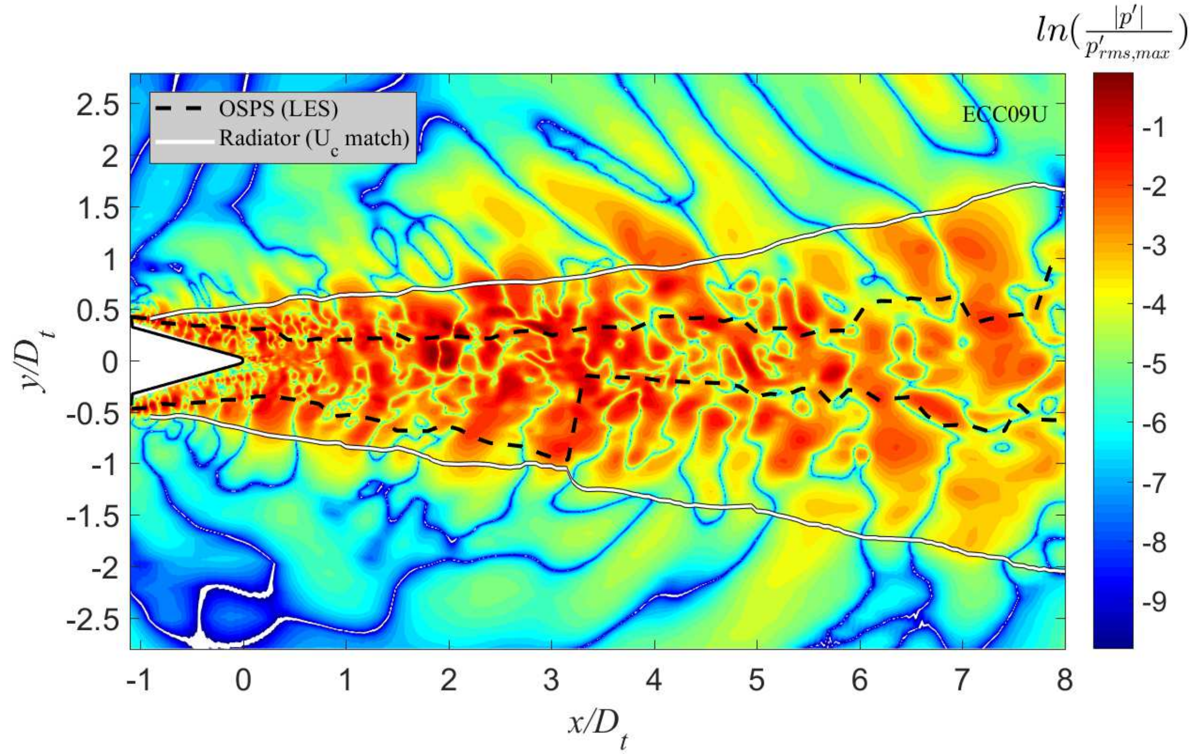

Figure 4.13: Distribution of the magnitude of the instantaneous pressure fluctuation of nozzle ECC09U, presented in normalized logarithmic form.

Chapter 5

Conclusion

5.1 Summary

Using large eddy simulations (LES) of two hot three-stream jets, key assumptions used in recent RANS-based volumetric modeling of jet noise source are assessed, and the proper location of a linear surface-based model is explored.

Of the jets studied, one is axisymmetric (nozzle AXI04U) and the other has an eccentricity of the tertiary, outer stream (nozzle ECC09U). The conditions simulated correspond to a supersonic turbofan engine at takeoff. The LES data used were arranged in azimuthal planes for a lower computational cost: six uniformly distributed meridional planes for nozzle AXI04U and the plane of symmetry for nozzle ECC09U. The simulation of nozzle AXI04U had relatively few time steps (885) of value $\Delta t = 5 \times 10^{-6} s$, so azimuthal averaging between planes was performed to improve the accuracy of the statistics. Nozzle ECC09U had a bigger number of time steps (2000) which allowed more time-averaged results, but azimuthal averaging was impossible due to three-dimensionality of the flow. The larger value of time step for ECC09U ($\Delta t = 10 \times 10^{-6} s$) made space-time correlations for the calculation of LES-based convective velocity slightly unreliable.

A new procedure for the detection of the relevant RANS-based surfaces is used. This avoids unrealistic results caused by steep azimuthal gradients when the search of the surfaces is performed radially. Instead, the procedure here applied searches for the surfaces following the traversal gradient of mean axial velocity, and procures more sensible results.

Direct evaluations of the Reynolds stress and convective velocity show that the RANS-based outer surfaces of peak stress (OSPS) and the modeled convective velocity along them are in good agreement with the LES results. In addition, examination of the instantaneous LES pressure fields indicate that the most energetic pressure events occur on the OSPS. These results lend credence to the use of the RANS-based OSPS to simulate the convective Mach number distribution in a multi-stream jet, one of the most critical decisions on the volumetric modeling.

The effort on the surface-based model focuses on the proper location of the "radiator surface", at the boundary between the rotational and irrotational fields, on which linear partial fields would represent the imprint of turbulent structures in the jet flow. The "conventional" definitions based on thresholds of the gradient of mean axial velocity show little difference between using $|\partial\overline{u}/\partial r|_{max}(x)$ as the outermost or absolute peak, although the former makes more physical sense. They are also sensitive to the threshold value used, making difficult the location of a unique surface.

As part of the effort on the surface-based model, the convective velocity U_c throughout the planes using space-time correlations of u' and p'. Both u' and p'-derived U_c fields show a sharp transition between hydrodynamic and acoustic fields, thus defining the "edge" of the jet, with the edge based on u' occurring outward relative to the edge based on p'. Conventional definitions place the radiator surface outside of both edges, thus fail to produce a surface with the desired property. A surface on which U_c is identical to that on the OSPS falls exactly on the edge of the jet based on the p' space-time correlation. This surface also appears to follow the outer band of a layer of negative pressure skewness, as has been observed in a cold single-stream jet,[43] but does not show a constant value of skewness along itself.

Although an exact definition of the radiator surface for multi-stream jets remains under investigation, the elements presented here offer intriguing prospects for further study of the phenomena at the edge of the multi-stream jet.

5.2 Recommendations for Future Work

The RANS and LES averaged flow fields used in this work show high levels of similarity, but are not a perfect match and.[46] The same work and methodologies founded in perfectly matching RANS and LES results would erase a big level of uncertainty in the disparity of the results.

The data processing for this work took many hours of computations done in a laptop computer, particularly for LES results. In order to spare resources in terms of storage and computational power, the LES data used was only in azimuthal planes: six for AXI04U, and two for ECC09U. In the future, using higher computational power can allow to use the full LES domain. This makes possible the application of azimuthal averaging of the relevant surfaces, avoiding singular errors and allowing for a wider interpretation of the phenomena studied.

The accurate and unique location of the radiator surface based on RANS information alone still remains under investigation. Future works should address this topic using as a reference the surface near the edge of the jet that has equal convective velocity based on p' space-time correlations, named U_c-match. Efforts should start by verifying if the U_c-match surface contains any particular characteristic such as a constant averaged magnitude, and validate it on different jets.

The exact physical meaning of the layer of negative skewness at the edge of the jet is still unknown. Future efforts may research further into this magnitude and its connection with noise generation and turbulence. Understanding this aspect may shed light on the connection of the U_c-match surface to RANS-based results and lead to a better understanding of jet noise emission.

Bibliography

[1] J. Seiner, "Advances in high speed jet aeroacoustics," *AIAA Paper 1984-2275*, Oct. 1984.

[2] D. Papamoschou, "New method for jet noise reduction in turbofan engines," *AIAA Journal*, vol. 42, no. 11, pp. 2245–2253, 2004.

[3] D. Papamoschou, "Modelling of noise reduction in complex multistream jets," *Journal of Fluid Mechanics*, vol. 834, pp. 555–559, Jan. 2018.

[4] C. Kish, "An estimate of the global impact of commercial aviation noise," Master's thesis, Massachusetts Institute of Technology, 2008.

[5] B. Molesworth and M. Burgess, "Improving intelligibility at a safety critical point: In flight cabin safety." *Safety Science*, vol. 51, pp. 11–16, 2012.

[6] M. Kaltenbach, C. Maschke, and R. Klinke, "Health consequences of aircraft noise," *Deutsches rzteblatt Int.*, vol. 105, no. 31-32, pp. 548–556, 2008.

[7] A. Adam, D. Papamoschou, J. Xiong, and F. Liu, "The very near pressure field of three-stream jets," *AIAA Paper 2018-1739*, jan 2018.

[8] C. K. W. Tam, "Stochastic model theory of broadband shock associated noise from supersonic jets," *Journal of Sound and Vibration*, vol. 116, no. 2, pp. 265–302, 1987.

[9] C. Tam, "Supersonic jet noise," *Annual Review of Fluid Mechanics*, vol. 27, pp. 17–43, 1995.

[10] C. Tam, M. Golebiowski, and J. Seiner, "On the two components of turbulent mixing noise from supersonic jets," *AIAA Paper 1996-1716*, May 1996.

[11] C. K. W. Tam, "Influence of nozzle geometry on the noise of high-speed jets," *AIAA Journal*, vol. 36, no. 8, pp. 1396–1400, 1998.

[12] M. Dahl and D. Papamoschou, "Analytical predictions and measurements of the noise radiated from supersonic coaxial jets," *AIAA Journal*, vol. 38, no. 4, pp. 584–591, 2000.

[13] K. Viswanathan, "Analysis of the two similarity components of turbulent mixing noise," *International Journal of Aeroacoustics*, vol. 3, pp. 43–46, 2002.

[14] K. Viswanathan, “Aeroacoustics of hot jets,” *Journal of Fluid Mechanics*, vol. 516, pp. 39–82, 2004.

[15] G. Brown and A. Roshko, “On density effects and large structure in turbulent mixing layers,” *Journal of Fluid Mechanics*, vol. 64, pp. 775–816, 1974.

[16] C. Tam and D. Burton, “Sound generation by the instability waves of supersonic flows. part 1. two-dimensional mixing layers,” *Journal of Fluid Mechanics*, vol. 138, pp. 241–279, 1984.

[17] C. Tam and D. Burton, “Sound generation by the instability waves of supersonic flows. part 2. axisymmetric jets,” *Journal of Fluid Mechanics*, vol. 138, pp. 273–295, 1984.

[18] D. Crighton and P. Huerre, “Shear-layer pressure fluctuations and superdirective acoustic sources,” *Journal of Fluid Mechanics*, vol. 220, pp. 355–368, 1990.

[19] D. McLaughlin, G. Morrison, and R. Troutt, “Experiments on the instability waves in a supersonic jet and their acoustic radiation,” *Journal of Fluid Mechanics*, vol. 69, pp. 73–95, 1975.

[20] R. Troutt and D. McLaughlin, “Experiments on the flow and acoustic properties of a moderate reynolds number supersonic jet,” *Journal of Fluid Mechanics*, vol. 116, pp. 123–156, 1982.

[21] C. K. W. Tam, K. Viswanathan, K. Ahuja, and J. Panda, “The sources of jet noise: Experimental evidence,” *AIAA Paper 2007-3641*, May 2007.

[22] D. Papamoschou and M. Debiasi, “Directional suppression of noise from a high-speed jet,” *AIAA Journal*, vol. 39, no. 3, pp. 380–387, 2001.

[23] B. Henderson, “Aeroacoustics of three-stream jets,” *AIAA Paper 2012-2159*, Jun. 2012.

[24] B. Henderson, S. Leib, and M. Wernet, “Measurements and predictions of the noise from three-stream jets,” *AIAA Paper 2015-3120*, Jan. 2015.

[25] D. Papamoschou, V. Phong, J. Xiong, and F. Liu, “Quiet nozzle concepts for three-stream jets,” *AIAA Paper 2016-0523*, Jan. 2016.

[26] M. Lighthill, “On sound generated aerodynamically: I. general theory,” *Proceedings of the Royal Society of London*, vol. 211, pp. 564–587, 1952.

[27] D. Papamoschou, J. Xiong, and F. Liu, “Towards a low-cost wavepacket model of the jet noise source,” *AIAA Paper 2015-1006*, Jan. 2015.

[28] C. Ho, “Near field pressure fluctuations in a circular jet,” *NASA CR-179847*, Nov. 1985.

[29] K. Zaman, “Flow field and near and far sound field of a subsonic jet,” *Journal of Sound and Vibration*, vol. 106, no. 1, pp. 1–16, 1986.

[30] D. Papamoschou, “On the connection between near and far pressure fields of a turbulent jet,” *AIAA Paper 2018-1251*, jan 2018.

[31] J. Mathieu and J. Scott, “An Introduction to Turbulent Flow.” Cambridge: Cambridge University Press, 2000, pp. 88, 354.

[32] B. S. Henderson and M. P. Wernet, “Characterization of three-stream jet flow fields,” *NASA/TM-2016-219098*, jul 2016.

[33] V. Phong and D. Papamoschou, “Investigation of isolated and installed three-stream jets from offset nozzles,” *AIAA Paper 2017-0005*, Jan. 2017.

[34] J. Xiong, A. Johnson, F. Liu, and D. Papamoschou, “Body force model for the aerodynamics of inclined perforated surfaces,” *AIAA Journal*, vol. 50, no. 11, pp. 2525–2535, 2012.

[35] D. Papamoschou, J. Xiong, and F. Liu, “Reduction of radiation efficiency in high-speed jets,” *AIAA Paper 2014-2619*, Jun. 2014.

[36] A. Jameson, W. Schmidt, and E. Turkel, “Numerical solutions of the euler equations by finite volume methods using Runge-Kutta time stepping schemes,” *AIAA Paper 1981-1259*, January 1981.

[37] F. Menter, “Two-equation eddy-viscosity turbulence models for engineering applications,” *AIAA Journal*, vol. 32, no. 8, pp. 1598–1605, 1994.

[38] J. Xiong, P. Nielsen, F. Liu, and D. Papamoschou, “Computation of high-speed coaxial jets with fan flow deflection,” *AIAA Journal*, vol. 48, no. 10, pp. 2249–2262, 2010.

[39] P. L. Roe, “Approximate riemann solvers, parameter vectors and difference schemes,” *Journal of Computational Physics*, vol. 46, no. 2, pp. 357–378, 1980.

[40] M. L. Shur, P. R. Spalart, and M. K. Strelets, “Noise prediction for increasingly complex jets. part i: Methods and tests,” *International Journal of Aeroacoustics*, vol. 4, no. 3, pp. 213–246, 2005.

[41] P. R. Spalart, W. H. Jou, M. Strelets, and S. R. Allmaras, “Comments on the feasibility of les for wings, and on a hybrid rans/les approach,” ser. 1st AFOSR Int. Conf. on DNS/LES, Ruston, LA, August 1997.

[42] P. R. Spalart and S. R. Allmaras, “A one-equation turbulence model for aerodynamic flows,” *AIAA Paper 1992-0439*, January 1992.

[43] D. Papamoschou and V. Phong, “The very near pressure field of single- and multi-stream jets,” *AIAA Paper 2017-0230*, Jan. 2017.

[44] A. Savitzky and M. J. E. Golay, “Smoothing and differentiation of data by simplified least squares procedures.” *Analytical Chemistry*, vol. 36, no. 8, pp. 1627–1639, 1964.

[45] K. Gee, T. Neilsen, and A. Atchley, “Skewness and shock formation in laboratory-scale supersonic jet data,” *Journal of the Acoustical Society of America*, vol. 133, pp. 491–497, May 2013.

[46] J. Xiong, F. Liu, and D. Papamoschou, “Large eddy simulation of three-stream jets,” *AIAA Paper 2018-1737*, jan 2018.